Statistical analysis of structures commonly used to determine palaeoflow within mass transport deposits

Mérolyn Camila NAVES DE LIMA RODRIGUES[a]*, Barbara TRZASKOS[a], G. Ian ALSOP[b,], Fernando FARIAS VESELY[a], Thammy Ellin MOTTIN[a], Danielle Cristine BUZATTO SCHEMIKO[a]

[a] Departamento de Geologia, Universidade Federal do Paraná, PO Box 19001, ZIP 81531-980, Curitiba, PR, Brazil; barbaratrzaskos@ufpr.br; vesely@ufpr.br; thammymottin@ufpr.br; danielleschemiko@gmail.com

[b] Department of Geology and Geophysics, School of Geosciences, University of Aberdeen, Aberdeen AB24 3UE, Scotland, UK; ian.alsop@abdn.ac.uk

*Corresponding author: merolyn.rodrigues@ufpr.br; - Basin Analysis Research Lab (LABAP), Centro Politécnico - Jardim das Américas, PO Box 19001, ZIP 81531-980, Curitiba, Paraná state, Brazil; Phone Number +55 41 3361-3306

Keywords: mass-transport deposits; syn-sedimentary deformation; original palaeoslope; Itararé Group; Paraná Basin

Abstract

Mass transport deposits (MTDs) contain deformation structures that are often used to determine the kinematics of palaeo-mass flows and hence the orientation of the original slope or gradient upon which the mass flow developed. When integrated with stratigraphic data, the azimuth of the palaeogradient can help elucidate the depositional evolution and palaeogeography of a region. However, most studies have defined palaeoslope from well-exposed MTDs, which raises some questions regarding the validity of establishing palaeoslopes where MTDs are poorly exposed. We examine MTDs of the Itararé Group (Paraná Basin), in southern Brazil, that are only partially exposed, but widely distributed both vertically and horizontally. Datasets and transport directions obtained from different structures, variable methods and multiple stratigraphic levels and geographic localities were statistically evaluated to verify the robustness of the methodology. This allows the orientation of local palaeoslopes to be established for different time intervals, even from disconnected outcrops. Faults and folds, that are the main structures used to define palaeoslopes, display the greatest potential to accurately determine transport direction in the examined MTDs. The use of other structures such as asymmetric boudins, quarter structures and injectites, helps to clarify flow kinematics. The integration of palaeoflow data with palaeocurrent data from associated deposits gives additional support for determining the orientation of the palaeoslope.

1. Introduction

Mass transport deposits (MTDs) derive from the collapse and downslope remobilization of rock and sediment via slides, slumps and debris flows (e.g., Martinsen 1994; Posamentier and Martinsen, 2011). As shear stresses originate from gravitational forces, deformation within MTDs is considered to reflect the orientation of the main parental slope. Therefore, flow kinematics deduced from ancient deposits can help to interpret sediment dispersal patterns and palaeogeography, particularly in deep water settings (e.g., Martinsen, 1994; Strachan and Alsop, 2006; Bull et al., 2009; Posamentier and Martinsen, 2011; Alsop et al., 2016; Sobiesiak et al., 2017; Jablonská et al., 2016, 2018).

Since the pioneering work of Jones (1939), several studies have employed folds and other soft-sediment structures generated by mass flow to define the orientation of palaeoslopes (e.g., Lewis, 1971; Woodcock, 1976a,b, 1979; Farrell, 1984; Maltman, 1984, 1994a,b; Debacker et al., 2001, 2009; Strachan and Alsop, 2006; Ogata et al., 2014b; Sharman et al., 2015; Alsop et al., 2016; Sobiesiak et al., 2016; Jablonská et al., 2018). Some of these studies have also discussed the usefulness and robustness of several different techniques to define slope directions (e.g., Woodcock, 1976a,b, 1979; Debacker et al., 2001, 2009; Strachan and Alsop, 2006; Alsop and Marco 2012; Sharman et al., 2015; Alsop and Weinberger, 2020).

However, the complex orientation and kinematics of MTD-related structures can complicate flow determination. For instance, folds can initiate at variable angles to flow including parallel, oblique and normal to the dip azimuth of the palaeoslope (Alsop et al. 2020). In addition, fold hinges and axial planes may subsequently rotate toward the transport direction and local backthrusts and folds verging upslope may also exist (e.g., Hansen, 1971; Woodcock, 1979; Farrell and Eaton, 1987; Strachan and Alsop, 2006;

Alsop et al., 2017). Further complications may include irregular palaeoslope and sea-floor topography, MTD frontal and lateral confinement and transport directions that change through time, together with overprinting relationships between adjacent MTDs, and other factors (e.g., Frey-Martinez et al. 2006; Gee et al., 1999; Bull et al., 2009; Alves and Cartwright, 2010; Ogata et al. 2019). Disaggregation and mixing of remobilized sediments may obliterate structures generated during earlier stages of the mass flow (Rodrigues et al., 2020). Furthermore, defining the palaeoflow of MTDs will also depend on data sampling and, therefore, ultimately on the degree of exposure (Debacker et al., 2009).

In order to test the accuracy and limitations of MTD structures as potential indicators of palaeoslopes, we have undertaken a systematic structural analysis of deformation from late Paleozoic MTDs that outcrop in the Paraná Basin (Itararé Group; southern Brazil). We then compare our results with a large published database of fluvial/deltaic and turbidite palaeocurrents from associated, undeformed strata. Besides applying several methods, the present study evaluates the robustness of structural datasets and the calculated transport directions obtained from each structure, thereby aiming to better understand the reliability and constraints of each set of structures.

2. Data and methods

2.1. Geological setting

This research was conducted in 17 outcrops of the Itararé Group (Fig. 1), which forms the glacially-related lower half of the Permo-carboniferous supersequence in the Paraná Basin (Holz et al., 2010). The studied MTDs cover three broad time intervals (Fig. 1), herein referred to as T1 (early Pennsylvanian), T2 (late Pennsylvanian) and

93 T3 (early Cisularian). These intervals correlate with the three palynozones as defined
94 by Souza (2006) and also correspond to previously defined formations (Schneider et
95 al.,1974; França and Potter, 1991).

96 The sediments of the Itararé Group largely accumulated in marginal to relatively
97 deep marine environments during multiple stages of deglaciation associated with the
98 late Paleozoic ice age in southwestern Gondwana (e.g., França and Potter, 1991;
99 Vesely and Assine, 2006). As the Itararé Group also contains evidence of glacio-
100 tectonism, localities for this study were carefully chosen to avoid direct glacial
101 influence. Typical glaciotectonised facies are restricted to where glacio-continental
102 strata lie on the preglacial substrate and are associated with subglacial diamicite
103 and/or glacially striated/grooved surfaces e.g., Fedorchuk et al, 2019; Rosa et al.,
104 2019). Our database is specifically derived from deltaic to offshore deposits where
105 direct glacial influence is absent.

106 After deposition of the Itararé Group, the Paraná Basin experienced several
107 tectonic events resulting from the reactivation of ancient basement faults by tensional
108 forces associated with the active margin of the South American Plate, and opening of
109 the Atlantic Ocean (e.g. Zalán et al., 1990; Soares, 1991; Milani, 1997, 2004). The
110 eastern flank of the Paraná basin, where this study is situated, was affected by
111 fracturing and basic magmatism during the opening of the South Atlantic and
112 subsequent evolution of the South American margin (Milani and Zalán, 1999). We
113 distinguish post-depositional tectonism from that related to mass-transport, as the
114 former manifests as subvertical fractures crosscutting multiple deposits (including
115 underlying and overlying sequences to the MTDs) and is associated with major fault
116 zones (e.g., Rostirolla et al., 2003; Trzaskos et al., 2006). Post-depositional tectonic
117 deformation is characterized by brittle features including fractures, cataclasites, and

deformation bands in sandstones. Furthermore, these structures commonly display transcurrent kinematics associated with the regional tectonic process, which are quite different to the kinematics indicated by mass-transport structures (for a general review into distinguishing tectonic from soft sediment deformation see Alsop et al., 2019).

In recent studies, deposition of MTDs in the Itararé Group have been associated with instabilities caused by high sedimentation rates linked with deglaciation (e.g., Suss et al., 2014; Carvalho and Vesely, 2017; Fallgatter and Paim, 2017; Valdez et al., 2017; Mottin et al., 2018) or rapid base-level fall due to isostatic rebound (Mottin et al., 2018). The patterns of sediment dispersal in the Itararé Group are relatively well known as several recent papers have reconstructed the paleogeography of the Paraná Basin and have produced a large amount of palaeocurrent, palaeo-ice flow and detrital provenance data (e.g., França et al., 1996; Gesicki et al., 2002; Vesely and Assine, 2006; Suss et al., 2014; Carvalho and Vesely, 2017; Fallgatter and Paim, 2017; Mottin et al., 2018). In general terms, sediment transport toward the NNW prevailed during T1 and T2, with local variations to the W and NE. This direction changed during T3, with palaeocurrents turning toward the SW in the central-northern sector of the basin, while in the south a more complex pattern started to operate feeding sediment centripetally into a subsiding area known as the “Rio do Sul” sub-basin (e.g., Castro, 1991).

Examined MTDs consist of large remobilized sedimentary blocks (intrabasinal clasts - IC), deformed slabs of sandstone, rhythmite and shale, and heterogeneous (banded) to homogeneous (massive) diamictites with IC. In a previous descriptive study, Rodrigues et al. (2020) grouped these into three main deformational facies (incipient – DF-1, mature – DF-2 and evolved – DF-3; Fig. 1 and Table 1). This was based on the relative proportion of coherent intrabasinal clasts and matrix, and on the

143 linkage between different structures, that indicate variable degrees and stages of mass
144 disaggregation and mixing during the flow. These deformational facies correspond,
145 respectively, to coherent slide to slump facies, slump to blocky-flow facies (with low
146 matrix content), and blocky-flow to debris-flow facies (with high matrix content) (e.g.,
147 Ogata et al., 2012a,b). The deformational facies do not seem to have a stratigraphic
148 relationship as they are developed during different time intervals (Fig. 1; Rodrigues et
149 al., 2020). The limits and thickness of a single MTD are usually difficult to assess due
150 to limited exposure of the Itararé Group. The thickness of the studied MTDs generally
151 ranges from about 5 m to 10s of meters (Carvalho and Vesely, 2017; Mottin et al.,
152 2018; Schemiko et al., 2019). Where exposed, boundaries between MTD and non-
153 MTD strata are sharp and the base of MTDs is usually erosive and irregular. The top
154 surfaces of MTDs, when identified, are generally flat but low amplitude relief is reported
155 locally, onto which overlying fine-grained facies may be ponded.

156 MTD-related structures include folds (Fig. 2A and B), faults (Fig. 2D to H),
157 injectites (Fig. 2I), asymmetric boudins (Fig. 2J), slickenlines along intrastratal
158 detachment surfaces, aligned intrabasinal and extrabasinal clasts (Fig. 2K),
159 grooves/scratch marks (Fig. 2L), sigma structures, quarter structures (Fig. 2M),
160 shearing features at the borders of intrabasinal clasts, and matrix banding (Fig. 2N).
161 Asymmetric folds associated with diapirs (here called diapiric folds; Fig. 2C) were also
162 studied. Although these diapiric folds are associated more with *in situ* deformation
163 rather than classic mass movement, they display preferential vergence. The rhythmite,
164 where these diapirs were developed, occurs under a fluvio-deltaic sandstone within a
165 sequence with little or no direct glacial influence (e.g., ?). Compressional and
166 extensional structures may occur in the same outcrop. Temporal relationships suggest
167 that folds generally predate faults and boudins, as they are often modified by the latter

two structures (e.g., Farrell 1984, Martinsen 1989, 1994, Martinsen & Bakken 1990, Strachan & Alsop 2006, Alsop & Marco 2014, Ogata et al. 2014a,b; Rodrigues et al., 2020

Location for Figs. 1 and 2.

Location for Table 1.

2.2. Characterization of structures and methods for palaeoflow definition

Structural orientation data, such as fold geometries (hinge plunges and trends, limb orientations, vergence and facing), fault orientation and kinematics, asymmetric boudin geometries (axis, faults and kinematics), kinematics of quarter structures and others (see Section 3.5. below) were measured in outcrops during field work and from oriented samples. Although some fold orientations were measured directly in the field, most hinge orientations (line of intersection of fold limbs or in a few cases the β or π axis; e.g., Fossen, 2016), axial plane orientations (the plane that bisects the fold limbs), fold facing orientations (Holdsworth, 1988) and interlimb angles were calculated stereographically.

Traditional classification schemes established in structural geology were employed for faults, boudins (Goscombe et al., 2004) and folds (e.g. Fleuty, 1964; Ramsay, 1967; for more information see Twiss and Moores, 2007; Fossen, 2016). In addition, we apply the flow perturbation fold model initially developed in metamorphic rocks (e.g., Holdsworth, 1990; Alsop and Holdsworth, 1993, 2007) but subsequently applied to folds in MTDs (e.g., Strachan and Alsop, 2006; Sobiesiak et al., 2016; Jablonská et al., 2018). This model considers that layer-parallel shear folds (LPS) are generated by velocity gradients in the downslope direction and layer-normal shear folds (LNS) are created by along-strike velocity gradients (Alsop et al., 2020). Some structures were named by importing non-generic terminology used to describe features

193 in ductile shear zones in metamorphic rocks (e.g., Passchier and Trouw, 2005; Ogata
194 et al., 2016).

195 The methods of palaeoslope definition were selected based on field observation
196 and analysis of stereographic projections. One or more methods were applied to each
197 kind of structure to define palaeoflow (Table 2; Fig. 3 to 6). For folds, at least one
198 method was applied for each structural element (hinge, axial plane and facing),
199 including mean axis method (MAM), downslope average axis method (DAM),
200 separation arc method (SAM), mean axial plane strike method (MAPS), mean axial-
201 planar dip method (MAD), axial-planar intersection method (AIM) and fold facing
202 direction (FFD), (Table 2; see also Alsop and Weinberger 2020 and references
203 therein).

204 Faults and asymmetric boudins containing faults were treated via the application
205 of the mean fault orientation method (MFOM and MFOM', respectively) and fault
206 intersection method (FIM and FIM', respectively) (Table 2; see also Debacker et al.,
207 2009). The mean orientation of slickenlines (SM) associated with faults is a
208 complementary method suggested in this research for faults (Table 2). For boudin
209 axes, we considered their orientation in relation to other features and hence the flow
210 direction (parallel or normal, see Table 2; Festa et al., 2013). Mean orientation of
211 slickenlines of intrastratal detachment surfaces, major axes of oriented extrabasinal
212 and intrabasinal clasts (based on Sobiesiak et al., 2016) and grooves/scratch marks
213 of intrabasinal clasts (based on Ogata et al., 2014b) have also been used to define the
214 mass-transport direction (Table 2). The orientation of injectites was also considered
215 with caution and based on their temporal and spatial relationship with other structures,
216 such as faults and folds. Injections may help identify the orientation of the extension
217 direction and with which MTD stage (initiation, translation, cessation and relaxation)

they are potentially related (Table 2). Therefore, injections may define if the extension is parallel, normal or oblique to the palaeoflow. The preferential orientation of bedding and banding in heterogeneous matrix was used for mean bedding strike method (MBSM; Table 2) as suggested by Sharman et al. (2015).

The transport direction obtained from each method applied to faults, folds, injectites and asymmetric boudins (axis and faults) were defined using the mean calculated vector (standard mean vector calculation). For this, a confidence interval of 95% (the semi-apical angle of confidence cone for a given confidence level) calculated on the Fisher Vector Distribution was applied (Woodcock and Naylor, 1983). Other structures, such as intrabasinal and extrabasinal clast orientations, slickenlines of intrastratal detachment surfaces and grooves/scratch marks in intrabasinal clasts, were plotted on rose diagrams and the transport direction was obtained through Von Mises distribution (Allmendinger et al., 2013; Cardozo and Allmendinger, 2013).

An average transport direction and respective confidence interval (95%) were obtained for each studied locality through Fisher Vector Distribution analysis of all transport directions established by the various methods used to define palaeoflow (Table 2). In a few cases, two possible transport directions were obtained due to alternative interpretations of some structures. The average transport directions were considered to be the mass-transport palaeoflow direction in the corresponding location. The kinematics indicated by fold, faults, quarter structures, shearing of intrabasinal clasts and SC-like structures, were also considered as palaeoflow indicators.

Published palaeocurrent data from the same region (Vesely and Assine, 2006, Suss et al., 2014; Fallgatter, 2015; Juk, 2016; Carvalho and Vesely, 2017; Fallgatter and Paim, 2017; Mottin et al., 2018; Schemiko et al., 2019) were used to compare the directions of sediment dispersal with MTD kinematics. These data include the dip

azimuth of cross-stratification in fluvial or fluvio-deltaic facies and the orientation of current ripples and flute casts in turbidites, both located in undeformed strata stratigraphically above and below the MTDs. The final calculated transport direction for each palaeoflow was compared with each other and with palaeocurrents from the same region and stratigraphic level to determine the robustness of the palaeoflow analysis.

Location for Table 2.

2.3. Statistical methods

Datasets of the different structures were statistically evaluated based on the amount of data, the preferential orientation (Woodcock and Naylor, 1983) according to the strength parameter C (Woodcock, 1977), and a confidence interval of 95% (see Appendix A). The amount of data was evaluated because some structural datasets comprise fewer measurements (less than 20) which can affect the reliability and robustness of the results. The strength parameter (C value) was obtained through structural geology software (such as: Stereo32 1.0.3 - Röller and Trepmann, 2003; and Stereonet 10.1.6 - Allmendinger, 2011) for datasets where N=5 or more measurements (minimum amount of data to obtain a C value) and calculated from eigenvalues defined by Bingham distributions (C = ln (eigenvalue 1/eigenvalue 3); Woodcock, 1977). The preferential orientation of each data cluster was defined from the strength parameter C (based on Woodcock and Naylor, 1983), which is here considered as none for $C \leq 1$, weak when $1 > C \leq 3$, moderate when $3 > C \leq 6$ and strong for $C > 6$. The final robustness classification of each structural dataset was obtained from the mode or mean (where no clear mode existed) of classification values given for the cited parameters (see Appendix A).

To evaluate the palaeoflow established by each kind of structure, we considered the number of methods and the confidence interval (95%) of the average palaeoflow defined from these various methods (see Appendix B). The evaluation of the final palaeoflow direction (corresponding to the parental palaeoslope) for each outcrop considered structural datasets (Appendix A), transport direction by structure (Appendix B), the total number of methods applied by outcrop (NM in Appendix B) and confidence intervals (95%) of the final transport direction (Appendix B). The final robustness classification of each palaeoflow direction by structure and final palaeoflow or palaeoslope direction in each outcrop were also obtained from the mode or mean of classification values given for the cited parameters (see Appendix A and B). The values used for classification represent the degrees of robustness of the evaluated parameters, structural datasets, structural transport direction and the final transport direction (more details in Appendixes A and B).

3. Analysis and results

3.1. Folds

3.1.1. Description and palaeoflow definition

Folds were classified as gentle to tight (based in Fleuty, 1964; Fig. 2A and B), rounded, cylindrical to gently curvilinear, and symmetrical or asymmetrical S or Z folds (Rodrigues et al., 2020; Fig. 2A-D). The variety of fold geometries, from simple to complex, identified during field work is highlighted for some selected cases (Fig. 3A-E). These cases are associated with progressive deformation and variable shearing associated with mass flow, which can be either parallel or at higher-angles (normal) to the flow direction.

3.1.1.1. Folds generated by LPS

Folds associated with layer-parallel shear (LPS) tend to display variable interlimb angles, cylindrical geometry and unimodal orientation data (hinge, axial plane and facing; Fig. 3A and 3B). The datasets range from symmetrical folds with gentle interlimb angles (Fig. 3A), to more complex folds (symmetrical to asymmetrical) with a fanning distribution of axial planar dips. Decreasing axial planar dips are associated with a reduction in interlimb angles and some hinge rotation (Fig. 3B). This variation in geometry and orientation seems to result from progressive deformation. In general, LPS fold hinges and axial planar strike are normal to the flow direction while fold facing is parallel to flow (see Alsop and Marco 2011). Thus, these folds were analysed through MAM, MAPS and FFD (Fig. 3A and 3B, and Table 2). MAD and MAD-AP were also applied to LPS folds with progressive deformation to avoid the influence of more rotated data (see Table 2) and confirmed the general flow trend indicated by other methods (Fig. 3B). MAD-AP also providerd a clear sense of flow that agrees with fold vergence (Fig. 3B).

3.1.1.2. Folds generated by LNS

Folds generated by LNS are characterized by bimodal orientation data (Table 2; more information in Table 1 of Alsop and Marco, 2011); however, the progressive deformation of these folds may also result in data rotation. Here, LNS folds tend to be asymmetrical, inclined to recumbent, and display variable interlimb angles and bimodality of at least 2 elements (e.g., axial plane and facing or hinge and facing - Fig. 3C and 3D, respectively) with little overlap of S and Z folds. The unimodality of one element (e.g., axial plane or hinge – Fig. 3C and 3D, respectively) and overlap between S and Z folds seem to be related to rotation of data possibly associated with some progressive deformation. In general, LNS folds show hinge trends and axial planar intersections sub-parallel to flow, with some axial planes striking oblique to flow and

317 fold facing generally normal to the flow direction (see Alsop and Marco 2011). Methods
318 applied include AIM, MAPS, FFD, DAM or SAM and, sometimes, MAM (Table 2 and
319 Fig. 3C and 3D). Hinge distribution of the recumbent folds (Fig. 3D) allowed the
320 application of SAM, which indicated a similar flow direction to MAM. Sub-horizontal
321 axial planes of the recumbent folds may not precisely indicate the flow direction and
322 results of MAPS may diverge from the main direction of flow (Fig. 3D). However, the
323 intersection between the mean axial planes of S and Z folds (AIM; Table 2) show a
324 more consistent flow direction (Fig. 3D). In other cases, MAPS was applied for all axial
325 plane data (S and Z folds); and although this may not represent the real axial plane
326 orientation of LNS folds, the dip direction of the mean axial plane is subparallel to AIM
327 (Fig. 3C).

328 *3.1.1.3. Diapiric folds*

329 Diapiric folds may show quite complex geometries and consequently display a
330 high data dispersion (Fig. 3E). However, some preferred orientation was identified (Fig.
331 3E), which indicates that most diapirs have an elongated shape. Elongated diapirs are
332 expected to be more or less parallel to the strike of the palaeoslope. The relationship
333 between interlimb angle and axial planar dip suggests a component of progressive
334 deformation (Fig. 3E), and may be evidence that these diapirs and diapiric folds
335 originated by local mass flows. For these folds, MAM, MAPS, FFD, MAD and MAD-AP
336 were applied and indicate similar flow directions (Fig. 3E).

337 *3.1.2. Statistical analysis*

338 In general, fold datasets tend to show variable dispersion independent of the
339 amount of data, as well as preferential orientation, confidence interval and robustness
340 (Table 3 and Fig. 3F). Yet, fold hinge, axial plane and fold facing datasets show roughly
341 similar preferential orientation and a narrow confidence interval (less than ± 20°) (Fig.

342 3F, Table 3 and 4). The ridges identified in folded injectite sills display a strong
343 preferential orientation, narrow confidence interval (95%) of ± 4.4° and are parallel to
344 fold hinges (Fig. 3D). The majority of averaged palaeoflow from folds show narrow
345 confidence intervals (less than ± 20°; Fig. 3G and Table 4) and were classified with
346 moderate to very strong robustness (Table 3 and Appendix B).

347 Location for Fig.3.

348 *3.2. Faults*

349 *3.2.1. Description and palaeoflow definition*

350 Faults occur as individual planes or clusters with straight, wavy or anastomosing
351 geometries (Fig. 2D-H), as well as reverse (Fig. 2D and 2H), normal (Fig. 2E and 2G)
352 or undefined kinematics, due to a lack of reliable markers (Rodrigues et al., 2020).
353 Some faults display sheared muddy cores of centimetric thickness, continuous clay
354 smear (Fig. 2F and 2H), discontinuous clay smear and form 'S-C' features (Fig. 2G;
355 Rodrigues et al., 2020). Normal faults typically show moderate dips with 'S-C' features
356 or anastomosing sets, up to high dip angles (Fig. 4A-4E). Faults with unclear
357 kinematics generally show moderate to low dip angles (Fig. 4D-4F), while reverse
358 faults usually show low to moderate dip angles (Fig. 4D-4F).

359 For faults with a single cluster, only the MFOM was applied (Fig. 4A and Table
360 2). Some datasets show conjugate faults with sub- to parallel strikes (Fig. 4B and 4F)
361 while others display oblique strikes (Fig. 4C), with faults that dip in opposing or two
362 different directions, respectively. In some localities we identified normal and reverse
363 faults with parallel to sub-parallel strike and opposing dip directions (Fig. 4D and 4E),
364 and unidentified faults with subparallel or oblique strike (Fig. 4D and 4E). For these
365 cases and the conjugate sets, MFOM was calculated for each cluster (Fig. 4B-4F). In
366 addition, FIM was estimated for the intersection of the conjugate sets and also between

367 the mean planes of the normal and reverse faults, which were interpreted to be normal
368 to the flow direction (Fig. 4D and 4E).

369 Slickenlines occur along some faults (Fig. 2F, 4C-4F), mainly in clay smear that
370 displays detachment surfaces or faults generated in mudstones. However, these may
371 not display clear kinematic indicators resulting in faults of unidentified kinematics (Fig.
372 4F). The mean orientation of the slickenlines was calculated and considered to be
373 parallel to the flow direction (Table 2 and Fig. 4C-4F).

374 *3.2.2. Statistical analysis*

375 Faults and slickenlines display variable dispersion, independent of the amount
376 of data; as well as, variable confidence intervals which tend to be narrow (less than ±
377 20°; Table 4 and Fig. 4G). The preferential orientation of faults is generally weak to
378 moderate, while it is weak for slickenlines (Table 3 and Appendix A). Fault average
379 transport direction shows variable confidence intervals, but are mostly narrow (less
380 than ± 20°; Fig. 4H and Table 4). Fault datasets were mostly classified with weak to
381 moderate robustness, while fault palaeoflows generally display moderate to very
382 strong robustness (Table 3, Appendix A and B).

383 Location for Fig.4.

384 *3.3. Injectites*

385 *3.3.1. Description and palaeoflow definition*

386 Injectites consist of sand injections that occur as dikes (Fig. 2I), with tabular to
387 anastomosing geometry or *en echelon* patterns, or tabular sills parallel to preserved
388 bedding or well-defined banded matrix (Fig. 2I; Rodrigues et al., 2020). The use of
389 injectites to define transport directions was applied to MTDs by Ogata et al. (2014),
390 and depends on their interpretation (how and when they were formed) and orientation
391 with respect to other structures.

In the MTD of locality 1, sills are folded together with banded matrix. The dikes that connect these sills (Fig 5A - dikes I; locality 1) show two main strike directions that are sub-parallel to each other with opposing dip directions and moderate to subvertical dip angles. A second phase of injection generated thin dikes (mm thickness; Fig. 5A – Dikes II) that cut the folded banded matrix, sills and early dikes (I) in locality 1. These dikes show a single main orientation and are subvertical (Fig. 5A). Comparing the orientation of the dikes I with folding, which is the main type of deformation in this MTD, it seems that dikes I originated either sub-parallel or sub-normal to the flow direction, while dikes II were generated normal to the flow direction.

Injectites parallel to continuous clay smear were observed in locality 8. These injectites consist of dikes that intruded the heterogeneous, banded matrix and display a clear preferred orientation with moderate dip angles (Fig. 5B). In this case, the injection was interpreted to occur normal to the flow direction as indicated by other structures. Other injectite datasets were collected in the MTD at locality 13 and consist of subvertical dikes associated with a few sub-horizontal sills (Fig. 5C). These dikes are more or less parallel to faults, oblique to folding and oblique to normal to the flow direction.

3.3.2. Statistical analysis

In our study, injectites show preferential orientation and quite narrow confidence intervals (95%; ±20° or less; Fig. 5D; Table 3; Appendix A). However, the confidence interval (95%) of the transport direction calculated from injectites ranges widely (Fig. 5E) due to the complexity displayed by some datasets (Fig. 5A-5C). The injectites show weak to strong robustness despite the weak preferred orientation, which indicates that data dispersion has no, or only limited, influence (Table 3 and Appendix A). Instead,

417 the robustness of injectite datasets is linked to the number of measurements (Fig. 5A-
418 5C; Appendix A).
419 Location for Fig. 5.
420 *3.4. Bedding and matrix banding*
421 *3.4.1. Description and palaeoflow definition*
422 The studied MTDs may show preserved bedding (Fig. 2B, 2C, 2E, 2J and 2M)
423 and/or matrix (Fig. 2A, 2D, 2F, 2G, 2H, 2I, 2K, 2L and 2N). The matrix can be
424 heterogeneous, with relicts of original bedding (Fig. 2A, 2G, 2I and 2N), or
425 homogeneous (Fig. 2D, 2F, 2H, 2K and 2L) (Rodrigues et al. 2020). The
426 heterogeneous matrix consists of mm-to dm-thick compositional/textural bands
427 (banded matrix) that can be well-defined (Figs. 2A and 2I) to subtle (Fig. 2N).
428 Bedding may reflect the orientation of the palaeoslope (Jones, 1939; Sharman
429 et al., 2015) and was therefore analysed in the present study, along with the orientation
430 of banded matrix. MBSM was applied to those MTDs with some preservation of
431 bedding or heterogenous matrix with compositional/textural banding (Table 2). When
432 bedding and banded matrix transport directions are compared to transport directions
433 derived from other structures (or average transport direction), both may sometimes
434 show considerable differences in orientation (Fig. 6A and Table 5). In the case study,
435 the use of the mean orientation of bedding or banded matrix (MBSM) resulted in little
436 or no significant change in the final transport direction (Fig. 6B and Table 5).
437 *3.4.2. Statistical analysis*
438 Both bedding and banded matrix show narrow confidence intervals (95%; up to
439 ±20°, Table 4), although bedding tends to display a better preferred orientation than
440 banded matrix (Fig. 6C, Table 3 and Appendix A). In terms of robustness, bedding and
441 banded matrix both tend to display datasets with moderate to strong robustness, while

the robustness of the transport direction is moderate for both (Table 3 and Appendix B). However, bedding shows the most datasets with strong robustness, while banded matrix datasets display mainly moderate robustness (Table 3 and Appendix A).

The weak preferential orientation of the banded matrix datasets is possibly related to the nature of the structures, which results from deformation and modification of the original bedding. The bedding datasets with weak preferential orientation may relate to data dispersion linked to deformation, such as folds associated with diapirs, LNS folds and normal faults (localities 3, 4 and 7, respectively; Appendix A). In some cases, the dispersion of data was compensated by a large number of data allowing the dataset to be classified as having strong robustness (e.g., locality 3; Appendix A).

The use of the mean orientation of bedding or banded matrix (MBSM) resulted in little or no significant change of the confidence interval of the final palaeoflow of each locality (Fig. 6D to E and Table 5).

Location for Fig. 6.

3.5. Other structural indicators

3.5.1. Description and palaeoflow definition

Other analysed structures include asymmetric boudins, slickenlines identified in intrastratal detachment surfaces, grooves and scratch marks, and intrabasinal and extrabasinal clasts. The asymmetric boudins (Fig. 2J) consist of shearband boudins (Rodrigues et al., 2020), which show backward vergence resulting from antithetic rotation with respect to shearing. Boudin faults show a preferred strike direction, which are more or less parallel to the boudin axis. These faults display normal and reverse kinematics and are distributed in two clusters of opposing dip directions, as result of gentle folding of the bedding containing these boudins. Both normal and reverse faults indicate kinematics towards the NW (Fig. 7A), which agrees with the flow direction

467 deduced from other kinematic indicators. Therefore, the extension that generated
468 these boudins was considered to be subparallel to the flow direction indicated by
469 normal faults (Fig. 4B) and so the boudin axis (MAM) and strike direction of boudin
470 faults (MFOM and FIM) is normal to the flow direction (Fig. 7A and Table 2).

471 The slickenlines of intrastratal detachment surfaces were developed along
472 shale laminations, or muddy laminations in rhythmites, and may be related to faulting
473 or folding (Rodrigues et al., 2020). These features show a main trend (Fig. 7B) that is
474 oblique in relation to palaeoflow from other structures analysed in the same MTD (Fig.
475 4B and 7A). The main trend for oriented clasts (elongated intra- and extrabasinal
476 granules to blocks; Rodrigues et al., 2020) (Fig. 2K) were defined through rose
477 diagrams of their major axes (e.g., Sobiesiak et al., 2016; Table 2). Both extrabasinal
478 and intrabasinal oriented clasts tend to show a main trend in the same MTD (Fig. 7C
479 and 7D, respectively), which is oblique in relation to each other (30°), but with general
480 E-W orientation. Intrabasinal clasts may also show deformation at their borders, such
481 as grooves and scratch marks (Fig. 2L; Rodrigues et al., 2020). These features were
482 analysed as axes on rose diagrams (as in Ogata et al., 2014b; Table 2), which indicate
483 a main trend (Fig. 7E) subparallel to palaeoflow of faults in the same MTD.

484 *3.5.2. Statistical analysis*

485 For these analysed structures, no robustness trend was defined due to the small
486 datasets (Fig. 7A to F, Table 3 and Appendix A). Between these structures, boudins
487 (Fig. 7A) seem to be the more reliable with moderate preferred orientation, moderate
488 dataset robustness and transport direction with strong robustness and narrow
489 confidence interval (95%; Fig. 7F, Table 3 and 4)

490 The other structures show confidence intervals (95%) a little larger than boudins
491 (Fig. 7F and Table 4), weak preferential orientation, datasets and transport direction

with weak to moderate robustness, of which the number of measurements tends to compensate the dispersion (Fig. 7B to 7E; Table 3; Appendix A and B).

Location for Fig. 7.

Location for Tables 3, 4 and 5.

4. Discussion

4.1. Do MTD structures show robustness for defining palaeoflows?

According to previous work, MTDs may show variations in palaeoflow due to several different situations associated with structural generation and modification during the flow, such as: i) difference in flow directions indicated by folds and thrusts at the lateral portions of MTDs (e.g. Alsop and Marco, 2012, 2013) or due to fanning of structures around the toe of MTDs (e.g. Strachan and Alsop, 2006; Alsop et al., 2020); ii) variable angles of fold initiation (Alsop and Marco, 2014); fold hinge and axial-planar rotation (Alsop and Marco, 2014); iii) overprinting between deformation of adjacent MTDs or between flow cells within individual MTDs (Alsop et al., 2020); among others. Some of these situations can be related to the development of structures in different domains of the MTD (extensional, translational, compressional and transcurrent) related to different regions of the flow (at the head, central, frontal or toe and lateral zones, respectively) and radial spreading of the flow (e.g., Alsop and Marco, 2012; Sharman et al., 2015). In addition, MTDs can be laterally confined or unconfined, and frontally confined or emergent (e.g., Frey-Martínez et al., 2006; Ogata et al., 2019). These conditions may result in lateral and vertical strain partitioning within the MTD that can create local variation of flow (Ogata et al., 2019).

Other local irregularities in the slope and sea-floor morphology can also result in variations of palaeoflow, such as: i) irregular morphology of previously deposited MTDs (e.g., Amerman et al., 2011; Alsop and Marco, 2014; Alves, 2015); ii) presence of

517 tectonic features like folds and faults (e.g., Dalla-Valle et al., 2015); iii) salt tectonics
518 (e.g., Alves and Cartwright, 2010); iv) mud diapirism (e.g., Alfaro and Holz, 2014); v)
519 variable orientation of the head scarp with respect to the intrabasinal slope gradient
520 (e.g., Armandita et al., 2015; Jablonská et al., 2016); vi) orientation and distance of the
521 locality of origin (i.e. structural highs or coastal areas) of a MTD with respect to the
522 depocenters (Ogata et al., 2012b). The limitations of MTD exposure resulting in non-
523 representative datasets may also result in different estimates of palaeoflow (Debacker
524 et al., 2009).

525 One main aspect of the studied area is the limited exposure that results in
526 disconnected or isolated outcrops. As this affects data collection and its
527 representativity, the different structural datasets and respective estimates of
528 palaeoflow were analysed statistically. The structural datasets and related palaeoflow
529 have variable robustness classification (Table 3, Appendixes A and B), but the majority
530 typically show moderate robustness. In several cases, the datasets tend to show weak
531 to moderate preferred orientation, which indicates data more or less dispersed and can
532 be related to the nature or complex geometry of the structures. However, data
533 dispersion tends to be compensated by number of data and the methods applied for
534 determining palaeoflow. In general, structural datasets and respective palaeoflow
535 show confidence intervals (95%) of less than 20° (Table 3; Appendix A and B; Fig. 3A,
536 3B, 4A, 4B, 5A, 5B, 6A and 7A). The confidence interval comprises the range of values
537 where the true mean orientation lies, and tends to be influenced by the data dispersion
538 and the number of measurements (e.g., Woodcock and Naylor, 1983). Therefore, we
539 consider that the main orientation of structural datasets and related palaeoflow may
540 vary 20° or less with respect to mean vectors obtained.

Faults and folds are the main structures in several studied outcrops and tend to show datasets and transport directions with moderate to strong robustness. Considering that they are also the most common structures in MTD, the robustness classification reassures their applicability in defining palaeoflows. Injectite datasets and palaeoflow may also show moderate to strong robustness. However, their applicability depends on the interpretation (how and when they were formed) and orientation with respect to other structures. Symmetrical and asymmetrical boudins are also relatively common in MTDs (e.g., Festa et al., 2013; Ogata et al., 2014b, 2016; Alsop et al., 2020; Rodrigues et al. 2020). Here, the dataset of asymmetric boudins have moderate and strong robustness, and a palaeoflow relatively close to palaeoflow estimated from other structures.

The weak preferential orientation and weak or moderate robustness of datasets and palaeoflow of the oriented clasts, and grooves/scratch marks on clast borders, is possibly related to the nature of these structures. These features are related to clasts dispersed in the matrix (diamictite) and, therefore, the data orientation depends on how shear is distributed within the matrix and how it affects the clasts (e.g., Ogata et al., 2014b; Sobiesiak et al., 2016). Transport directions estimated from the intrastratal slickenlines, oriented clasts, and grooves and scratch marks are slightly oblique to oblique to folds and/or faults in the same MTDs. Although these features are less common, their analysis may be an important complementary method for palaeoflow definition, or even the main method in cases where folds and faults are lacking, as in some debris flows (evolved MTDs - DF-3). However, as there are few datasets where intrastratal slickenlines, oriented clasts, grooves and scratch marks and boudins were analysed, further studies are required to verify their applicability in defining palaeoflows.

In more or less coherent/cohesive MTDs (slide/slump to blocky-flow - DF-1 and DF-2), bedding orientations are relatively easy to collect data, while within diamictite MTDs (debris flow - DF-3) banded matrix can be an important feature that acts as a marker for other deformation (folds, faults, and others). In some localities, tilted bedding and banded matrix may be the main features indicative of deformation in the MTD. Therefore, we suggest that they should be analysed with caution, and preferably only in combination with other structural data for palaeoflow analysis.

The palaeoflows indicated by different structures in the same MTD outcrop may be parallel or normal (Fig. 8A); however, in most cases the palaeoflows tend to be parallel to oblique (≤45°). These include outcrops with two or more analysed structures; for the latter case the angular relationship between palaeoflows may vary little or widely. In most outcrops, no clear lateral or vertical variation of structural distribution and orientation were identified. Alternatively, the compared palaeoflows may be obtained from structures that occur in the same interval of an outcrop. The palaeoflow of the MTD from outcrop 4 is the only transport direction defined from structural datasets analysed in two different intervals of one MTD, that include the lower (base; including overlapping interval deformed at the contact) and median intervals (middle). In general, the palaeoflows from different structures are slightly oblique, ranging from parallel to oblique. However, at the base interval the palaeoflows from faults and folds are parallel with each other and oblique to the bedding palaeoflow. While in the middle interval, the palaeoflow from different structures are parallel to subparallel. The resulting palaeoflow corresponds to the ‘general’ or main palaeoflow (toward 240°) for the MTD at locality 4 (Fig. 9). Whereas, when each interval is analysed separately the resulting palaeoflows are slightly oblique (toward 250° and 229° at the base and middle

intervals, respectively) and indicate a vertical variation of flow within the MTD, although both show a general trend toward the SW.

Strain variations within the MTD created during the flow may be associated with slope and sea-floor morphology (e.g. Ogata et al., 2019), together with modification and rotation of structures during flow (e.g., Alsop and Marco, 2012, 2013, 2014). The nature and/or geometry of structures such as oriented clasts depends on shear distribution in the matrix (e.g., Ogata et al., 2014b; Sobiesiak et al., 2016) and may also explain the variations of palaeoflow indicated by different structures.

The vertical variation of palaeoflow identified in the MTD of locality 4 suggests a vertical strain partitioning related to vertical difference of flow and shearing as a result of the style of basal interaction beneath the MTD (e.g., Cardona et al., 2020). The interaction between the base interval of the MTD at locality 4 and the overlying deposit is similar to continuous no-slip substrate deformation of Sobiesiak et al. (2018), which may result in differences of shear stress, flow velocity and direction between the basal, middle and upper interval of a MTD (e.g., Strachan, 2008; Cardona et al., 2020). Most of the strain during mass flow is believed to accumulate where maximum shear stress develops at the basal interval (e.g. Middleton and Hampton, 1976; Elverhøi et al., 1997). However, the representativity of datasets of some structures must be considered in some cases. Here, the evaluation of structures and related palaeoflow robustness through the number of data, preferential orientation, and number of methods may help qualify the representativity of some datasets.

Simple models of MTDs consider that the head (extensional) and toe (contractional) zones show relatively uniform displacement along the strike of the structure related to layer-parallel shear (LPS), while the lateral margins are marked by pronounced along-strike variation in displacement related to layer-normal shear (LNS)

615 (e.g., Farrell, 1984; Farrell and Eaton, 1987; Alsop and Marco, 2011, 2014; Armandita
616 et al., 2015; Alsop et al., 2020). Although folds at two outcrop localities (localities 1 and
617 4) were identified as being the result of LNS, the criteria for recognizing lateral margins
618 of MTDs proposed by Debacker et al. (2009) are not satisfied by the limited dataset of
619 folds and/or faults. In addition, MTDs may develop secondary flow cells related to
620 variations in rates of downslope movement, which may generate local areas of LNS
621 within MTDs (Alsop and Marco, 2014). Therefore, lateral margins of MTDs were not
622 identified due to the limited exposure of outcrops.

623 In general, the application of as many methods as possible will better constrain
624 the palaeoslope from MTD structures (e.g. Woodcock, 1979; Strachan and Alsop,
625 2006; Debacker et al., 2009; Alsop and Marco, 2012; Sharman et al., 2015).
626 Furthermore, some studies have concluded that the analysis of more than one kind of
627 structure also improves the reliability of palaeoslope definition (e.g. Debacker et al.,
628 2009; Sharman et al. 2015). Through a careful analysis of the geometry, spatial
629 relationships and kinematics of the structures, and the application of several methods
630 at the same locality, it was possible to obtain reasonable estimates of palaeoflow.
631 However, due to the limited exposure it was not possible to study different portions or
632 the MTDs as a whole. Therefore, the palaeoflow obtained in each locality is considered
633 a local trend of the respective MTD. These palaeoflows display mostly narrow
634 confidence (70% with confidence interval 95% of ±20° or less; Fig. 8B) and moderate
635 robustness (about 70%; Fig. 9 and Appendix B). The number of structures analysed
636 and methods applied compensated the number and/or dispersion of data, the
637 complexity of deformation and variation of palaeoflow obtained from each structure.

638 The palaeoflow of different MTD outcrops in the same region and stratigraphic
639 level may display similar general trends. Within the T1 interval, localities 4 and 5 show

MTDs with oblique palaeoflows, yet they show moderate robustness and indicate a general flow towards the W (Fig. 9). The MTD of locality 6 revealed a palaeoflow with moderate robustness towards the SW, which is slightly oblique to the palaeoflow direction obtained by Amato (2017) using anisotropy of magnetic susceptibility (AMS) in the same diamictite (Fig. 9). Two MTD localities (3 and 8) within T2 were analysed in the northern and central regions of the studied outcrop belt respectively. Both MTDs show good robustness (locality 3 with strong and locality 8 moderate robustness) and a general flow towards the N (NE and NNW, respectively), though the localities are positioned several hundreds of km apart (Fig. 9).

In the northern region, two separate MTD units (localities 1 and 2) from the T3 interval have slightly oblique palaeoflows, with a general transport direction towards the SW (Fig. 9), both with moderate robustness. Within T3 in the central region, locality 7 show asymmetric folds and sigma structures (sheared intrabasinal clasts) that suggest a mass-flow direction to the SW (Fig. 9). However, this palaeoflow is considered non-robust, as fewer structures were described and these are inaccessible for direct measurement. On the other hand, at locality 9, the inferred palaeoflow direction is toward the NE and this shows strong robustness.

In the southern region (between Aurora and Witmarsum; Fig 9), MTDs from localities 10 to 12 (T3 interval) have palaeoflows with moderate to strong robustness ranging from the NE and NW that suggest a general flow towards the N. The AMS results from Amato (2017) for the MTD of locality 12 also indicate palaeoflow toward NNW, which is oblique (<45°) to the palaeoflow defined from structures. MTDs from localities 13 to 17 (T3 interval), further to the south, display a radial palaeoflow pattern ranging from WNW to SW (Fig. 9) with mostly moderate robustness, which indicate a

general trend towards the W in agreement with other MTD palaeflows derived from AMS data (Amato, 2017).

Considering that each MTD outcrop palaeoflow corresponds to a local transport direction, the variations of palaeoflow between MTDs in the same region and stratigraphic interval may result from the different factors and conditions previously cited. This includes structural generation and modification during the flow in different regions of the MTD and conditions of confinement, which may result in lateral and/or vertical strain partitioning (e.g., Frey-Martínez et al., 2006; Strachan and Alsop, 2006; Alsop and Marco, 2012, 2013, 2014; Sharman et al., 2015; Ogata et al., 2016, 2019; Sobiesiak et al., 2016; Alsop et al. 2020). These variations in palaeoflow can result from local irregularities in the slope and sea-floor morphology (e.g., Amerman et al., 2011; Ogata et al., 2012b, 2019; Alsop and Marco, 2014; Alves, 2015; Dalla-Valle et al., 2015; Jablonská et al., 2016). Dataset representativity related to limitations of MTD exposure were qualified through statistical analysis, which may explain some of the wider divergences in estimated palaeoflow identified between MTDs in the same region and stratigraphic level (i.e., localities 7 and 9). Nevertheless, the close orientation between palaeoflows of different MTDs in the same region and stratigraphic interval may represent the general gradient of the palaeoslope or sea-floor with respect to the depocenter. Therefore, this possibility must also be considered, especially in palaeogeographical studies.

With regard to the deformational facies, though the coherent slide MTD (incipient – DF 1) of locality 15 shows a palaeoflow with weak robustness due to the small dataset, no clear relationship between the robustness of data and flows was identified. However, the palaeoflow definition may depend on the diversity and amount of deformation structures within the MTD, which is related to the degree of deformation

689 and disaggregation of the remobilized sediments (e.g., Martinsen, 1994; Ogata et al.,
690 2012a). Slumps (incipient - DF-1 and mature – DF-2) and blocky-flows (mature - DF-2
691 and evolved – DF-3) tend to show a large amount and variety of structures compared
692 to slides due to degree of deformation. Blocky-flows rich in matrix and debris flows
693 (evolved DF-3) also tend to show a large variety of structures, but smaller amounts as
694 sediment disaggregation may obliterate initially formed structures.
695 Location for Fig. 8.
696 *4.1.1. Folds versus faults, which is more reliable and robust for palaeoflow definition?*
697 Folds are the most commonly used structure to define palaeoslope from MTDs
698 and are generally considered the most reliable (e.g., Jones, 1939; Woodcock, 1979;
699 Strachan and Alsop, 2006; Debacker et al., 2009; Alsop and Marco, 2012; Ogata et
700 al., 2014b; Sharman et al., 2015; Alsop et al., 2016; Sobiesiak et al. 2016; Jablonská
701 et al., 2018; Naji et al., 2018). Faults are the second most commonly used structure to
702 define palaeoslope (e.g., Farrell, 1984; Debacker et al., 2009; Ogata et al., 2014b;
703 Sharman et al., 2015; Alsop et al., 2016; Jablonská et al., 2016, 2018; Sobiesiak et al.,
704 2016).
705 The palaeoflow orientation obtained from folds shows confidence intervals with
706 similar ranges to the palaeoflow derived from faults, with both cases being derived from
707 one or more methods (Table 4). Datasets of fault and fold elements show similar
708 degrees of preferred orientation and confidence (Table 3; Fig. 3F and 4G). However,
709 techniques to determine palaeoflow using folds display narrow confidence intervals
710 (Fig. 3G) compared to faults (Fig. 4H).
711 Both folds and faults also show similar and variable datasets and palaeoflow
712 robustness, although faults are slightly more robust than folds (Table 3). The geometry
713 of folds and their associated complexity has no clear influence on the robustness of

714 the dataset or palaeoflow; however, the combination of preferential orientation and the
715 number of measurements is important for the reliability of the results. Some datasets
716 of different kinds of folds show similar robustness, such as the simple LPS upright
717 symmetrical folds of locality 17 and the more complex LNS folds of locality 1 (Fig. 3A
718 and 3C, respectively; Appendix A). However, the palaeoflow of localities 1 and 17 show
719 strong and moderate robustness, respectively (Appendix B). Furthermore, folds of
720 locality 11 (Fig. 3D) show a similar number of measurements and dataset robustness
721 to locality 17, but palaeoflow displays strong robustness against moderate robustness
722 of locality 11 (Appendix A and B). These variabilities seem to relate to the number of
723 methods applied rather the number of measurements. Alternatively, the diapiric folds
724 of locality 3 (Fig. 3E) show strong robustness despite a lower preferential orientation
725 compared, for instance, with the folds of localities 13 and 17 with moderate robustness
726 (Fig. 3A and 3B). This seems to be the result of a larger dataset that compensated for
727 the weak preferred orientation (Appendix A). Although more complex folds (as from
728 locality 1 and 3, Fig. 3C and E) tend to show weaker preferred orientation than simple
729 folds (as from locality 13 and 17, Fig. 3A and 3B), more methods can be applied to the
730 complex folds. Many authors recommend the application of several techniques (e.g.,
731 Debacker et al., 2009; Alsop and Marco, 2012; Sharman et al., 2015), and this
732 increased number of methods may control the confidence interval (95%).

733 Fault datasets and palaeoflow robustness is controlled by the number of data
734 and preferential orientation associated with geometry (as straight and subparallel,
735 conjugated, anastomosing clusters), instead of kinematics (normal, reverse or
736 undefined; Fig. 4A-4F; Appendix A). Fault sets with simpler patterns tend to show
737 better robustness, such as faults from localities 10 (Fig. 4B) and 17 (Fig. 4A) compared
738 to faults of locality 16 (Fig. 4C). However, fewer methods can be applied to some

739 simpler datasets (as from locality 17; Fig. 4A) when compared to more complex
740 datasets (as from localities 9 and 12; Fig. 4D and 4E), and this may affect the
741 robustness of the transport direction and its confidence interval.

742 Faults generally seem to be an easier structure to analyse compared to folds,
743 and methods of fault analysis typically indicate a broad transport sense (cf. Debacker
744 et al., 2009). Normal faults within the toe and central zone of MTDs tend to be at high
745 angles to the transport direction, but may also be generated parallel to flow (Alsop and
746 Marco, 2011). Folds on the other hand may show complex orientation patterns and
747 require careful analysis and, even then, may result in more than one interpretation.
748 This can be related to several factors, such as variable angles of fold initiation, variable
749 amounts of fold hinge and axial plane rotation, interaction between adjacent MTDs
750 (Alsop et al., 2020), second-order flow cells (see Alsop and Marco, 2014), and variable
751 gradient or transport directions that may change with time (Alsop et al., 2020).

752 The orientation of faults and folds with respect to each other was analysed using
753 a different approach. For cases where folds show more than one possible
754 interpretation, we analysed their orientation with respect to normal and reverse faults
755 that share parallel strikes and opposing dip directions. This arrangement of faults is
756 here considered more likely to represent the sense and direction of transport, where
757 the fault strike is sub- parallel to the gradient strike. This analysis allowed us to reduce
758 the possible interpretation for folds in the same locality, as well as, to define with more
759 confidence the sense and direction of transport even in localities where just faults were
760 identified.

761 By comparing the orientation of palaeoflow derived from faults and folds from the
762 same locality, we verified a wide range of differences in orientation (Fig. 4I). However,
763 in most cases this angle is less than 30° (Fig. 4I), therefore most folds and faults

palaeoflow are parallel or only slightly oblique to one another. These difference in orientation may result from structural generation and modification during the flow (e.g., Frey-Martínez et al., 2006; Strachan and Alsop, 2006; Alsop and Marco, 2012, 2013; Ogata et al., 2019; Alsop et al., 2020), which can be influenced by local irregularities in the slope and sea-floor morphology (e.g., Alves and Cartwright, 2010; Amerman et al., 2011; Ogata et al., 2012; Alsop and Marco, 2014; Alves, 2015; Armandita et al., 2015; Dalla-Valle et al., 2015; Jablonská et al., 2016).

Based on all these observations, the conclusion is that, in general, folds and faults display similar quality and robustness. Differences in robustness and palaeoflow orientation between these structures may depend on sampling (e.g., Debacker et al., 2009), which may affect the interpretation. Careful analysis of structures permits the palaeoflow to be obtained with equal significance from both structures. However, as fold geometry is more complex than faults, the selection of appropriate methods of palaeoflow definition may be more difficult for folds.

4.2. Meaning of MTD palaeoflow for palaeographic studies

Several studies have defined the orientation of a parental palaeoslope by using MTD structures (e.g., Farrell, 1984; Farrell and Eaton, 1987; Martinsen, 1989; Strachan and Alsop, 2006; Debacker et al., 2009; Alsop and Marco, 2012; Sharman et al., 2015; Alsop et al., 2016; Jablonská et al., 2016, 2018; Naji et al. 2018).However, MTDs may show a main flow direction combined with local variations related to different factors, such as the previously mentioned structural generation and modification and/or slope and sea-floor morphology (Fig. 10) (e.g., Strachan and Alsop, 2006; Alves and Cartwright, 2009; Ogata et al., 2012b; Alfaro and Holz, 2014; Alsop and Marco, 2014; Alves, 2015; Dalla-Valle et al., 2015; Jablonská et al., 2016;

789 Ogata et al., 2019; Alsop et al., 2020). For instance, some studies demonstrate that
790 regional variation of MTDs palaeoflow within the same stratigraphic level is associated
791 with palaeogeography and palaeoslope orientation (e.g., Alsop and Marco, 2012).
792 Regional to local variation of MTDs palaeoflow through a sequence in the same
793 stratigraphic level may reflect temporal or spatial changes in flow, or the sampling of
794 variably oriented structures associated with the frontal and lateral margins of broadly
795 elliptical-shaped failures (Alsop et al., 2020).

796 MTDs can result from gravitational mass flows with long runout distances (e.g.,
797 Elverhøi et al., 2002; Lamarche et al., 2008; De Blasio and Elverhøi, 2011). Such flows
798 may lose the influence of palaeoslope azimuth and reorient because of sea-floor
799 topography or depocenter location (Fig. 10) (e.g., Gee et al., 1999; Bull et al., 2009;
800 Alves and Cartwright, 2010). They may travel over more or less flat areas of the
801 seafloor (e.g., Lamarche et al., 2008; Joanne et al., 2013), or even show some upslope
802 movement (i.e., in the toe region) due to flow towards an obstacle (Fig. 10) (i.e., mud
803 diapir; e.g., Alfaro and Holz, 2014). Therefore, MTD flow may or not represent the
804 palaeoslope azimuth, as well as other gradients related to the slope and/or seafloor
805 morphology (Fig. 10). When gravitational mass flows are transported (partially or
806 totally) down gentle gradients and over flatter areas, the flow direction may or may not
807 indicate the original slope. This will depend on various situations, such as: lateral
808 confinement of the mass flow (e.g., Ogata et al., 2019); presence of obstacles (i.e.,
809 structural highs, mud or salt diapirs, and others) that may change the flow direction
810 (e.g., Storegga Slide; Lamarche et al., 2008; Dalla-Valle et al., 2015). The
811 coherency/cohesion of mass flows which may vary from slides and slumps to less
812 coherent debris flows (e.g., Ogata et al., 2012a), may result in less coherent mass
813 flows spreading more easily in the downslope toe zone, or in non-confined areas

814 (e.g.,Lucente and Pini, 2003; Frey-Martinez et al., 2006; Lamarche et al., 2008; Bull et
815 al. 2009).

816 As individual MTDs may show variation in palaeoflow, it is advisible to consider
817 the palaeoflow as an indicator of local gradient rather than using it to define the regional
818 slope. The definition of the regional gradient requires the study of several MTDs in the
819 same region and stratigraphical interval, together with stratigraphic data (such as
820 paleocurrents, facies association, contact with other deposits) and, when possible,
821 tectonic data, as tectonic structures may have been active during deposition of MTDs.
822 Only a few studies have integrated MTD structures with paleocurrents of associated
823 deposits, for example, to better define the palaeoslope and its paleogeographic
824 implications (e.g., Strachan and Alsop, 2006).

825 Where MTDs are well-exposed, the collection of structural data from different
826 parts of the same MTD may allow a consistent definition of palaeoflow and related local
827 palaeoslope. However, where MTDs are exposed in disconnected or isolated outcrops,
828 as is the case of the present study, it is usually impracticable to analyse each of them
829 as a whole or even different parts of an MTD. In such cases, we suggest that each
830 outcrop dataset is analysed separately; and the data then integrated between different
831 outcrops that can be correlated. The palaeoflow results obtained in each MTD outcrop
832 should be considered as local indicators that may represent the local palaeoslope. In
833 this scenario, the study of several outcrops of MTDs, within a region and similar
834 stratigraphic level, together with the evaluation of datasets and respective palaeoflow
835 robustness, may help to define the regional palaeoslope and local variations with some
836 reliability. The results allow some general inferences about the palaeogeography and
837 palaeogeomorphology, although the origin of variations in palaeoflow such as flow

838 blocking by structural or frontal/lateral confinement will depend on the amount of
839 exposure.

840 In some regions and stratigraphic intervals studied here, there are few MTD
841 outcrops with preserved structures (outcrop localities: 4, 5 and 6 in T1; 3 and 8 in T2;
842 7 and 9 in T3), so for these cases it is not possible to infer the orientation of the regional
843 palaeoslope or seafloor. Even so, the palaeoflow of most of these MTDs outcrops is
844 considered to reliably indicate the local palaeoslope, with the datasets showing mostly
845 moderate robustness. In the region of Alto do Amparo, localities 4 and 5 within the T1
846 interval (Fig. 9) palaeoflows with a normal to slightly oblique orientation with respect to
847 nearby turbidites. These turbidites show palaeocurrents mostly towards the NW with
848 some NE dispersion, that may be related to irregularities of the palaeomorphology
849 (Juk, 2016). Considering that MTD of locality 5 is overlain by MTD outcrop 4 and both
850 were locally analysed, the difference in palaeoflow between these two MTD outcrops
851 can be the result of irregular physiography, which could be created by MTD 5.
852 However, these differences in palaeoflow may also relate to other aspects including
853 internal flow variations related to structural generation and modification within different
854 portions of the MTD (e.g., Alsop et al. 2020), conditions of confinement of the
855 sediments during the flow (e.g., Ogata et al., 2019), and limited data collection (e.g.,
856 Debacker et al., 2009). Although, no variation in structural orientation or evidence of
857 confinement was identified, a general trend towards the W can be indicated for the
858 local palaeoslope. Further south, the MTD of locality 6 within T1 (Fig. 9) shows
859 palaeoflow toward the SW that diverges widely from palaeocurrents in the fluvial-
860 deltaic deposits in the surrounding area, that indicate flows going towards the N and
861 NW (Beraldin, 2014; Rosa et al., 2019). This divergence in orientation may indicate

862 some local variation in the palaeomorphology, although further investigation is
863 required.

864 The local palaeoflow of MTD 8 (within T2; Fig. 9) is subparallel or slightly oblique
865 to palaeocurrents indicated by cross-stratified sandstones interpreted as proglacial
866 fluvial and delta-plain deposits (Suss et al., 2014; Carvalho and Vesely, 2017).
867 According to Carvalho and Vesely (2017), the MTDs (commonly containing sandstone
868 blocks of fluvial and deltaic origin) result from mass-failures triggered by sediment
869 supply and loading. This develops during base-level rise and is related to progradation
870 of deltaic systems (e.g., Suss et al., 2014) with stacking patterns indicative of normal
871 regression. The general similarity between the palaeoflow of MTD 8 and the fluvio-
872 deltaic palaeocurrents may indicate that the mass-flow was influenced by the deltaic
873 clinoform at the studied locality.

874 At locality 3, the local palaeoflow indicated by diapiric folds in rhythmite (within
875 T2; Fig. 9) is oblique or normal to palaeocurrents of proglacial fluvial and delta-plain
876 deposits that lie directly on the deformed deposit (Vesely and Assine, 2006). Although
877 it is not a fully-developed MTD, folds in this deformed deposit show vergence toward
878 the N and NE and suggest a local mass movement. The difference in flow orientation
879 with palaeocurrents may be related to the nature and development of the diapiric folds,
880 which may not precisely reflect the palaeoslope, and/or data collection being limited to
881 the exposure area. These diapiric folds are considered to result from local shear
882 stresses influenced by loading.

883 Within the T3 interval in the central region of the studied outcrop belt, MTDs of
884 localities 7 and 9 show an opposed palaeoflow direction towards the SW and NE,
885 respectively (Fig. 9), The palaeoflow of MTD 9 is much more reliable than MTD 7 as it
886 displays a strong robustness compared to the non-robust MTD 7. However, fluvio-

887 deltaic palaeocurrents near locality 9 are not available for this time interval. The nearest
888 data are westward-directed current ripples and flute casts from underlying turbidites
889 which are exposed 60 km to southwest, and which were deposited on a west-directed
890 slope (Fallgatter, 2015). The distance between these deposits weakens any
891 correlations, which are also complicated by the MTD palaeoflow being influenced by
892 the previously cited situations such as irregular physiography and data collection.

893 The correlation between palaeoflow of MTDs and information gained from the
894 depositional evolution of adjacent sediments may allow inferences about the regional
895 palaeoslope to be made, even where few cases were analysed. MTDs of localities 1
896 and 2, in the northern region (within T3; Fig. 9) show palaeoflows that are in agreement
897 with palaeocurrents from outwash and fluvio-deltaic facies formed both below and
898 above the MTDs (Mottin et al., 2018). Both outcrops are part of the stratigraphical and
899 palaeogeographical study presented by Mottin et al. (2018). These authors suggest
900 that the emplacement of mass-transport deposits at different times results from
901 instabilities related to isostatically-driven tectonic forces and associated base-level fall
902 that caused the remobilization of previously accumulated glaciomarine deposits.
903 Although, the palaeoflow of MTDs represents the local palaeoslope, the similarity of
904 flow with other associated deposits allows us to suggest a general palaeoslope toward
905 SW for that particular interval.

906 Several outcrops of different MTDs from the T3 interval were analysed in the
907 southern region (between Witmarsum and Alfredo Wagner; Fig. 9) and significant
908 variation in the orientation of palaeoflows was identified, most of them with moderate
909 robustness. Although a larger number of MTD outcrops would be more revealing for
910 such a large region, some patterns emerged and suggest the main trends for the
911 northern and southern portions of the region. Within this interval, all outcrops (except

912 for locality 11) are placed above the Lontras shale and may comprise a MTC (mass
913 transport complex, sensu Ogata et al., 2014a) in the upper Rio do Sul Formation.
914 These MTDs can be divided in three groups of observed palaeoflow patterns, namely,
915 from south to north: ranging from SW to the WNW (localities 13 to 17), to the NW and
916 NE (localities 10 and 12) (Fig. 9). The MTD of locality 11, below the Lontras Shale,
917 shows paleoflow toward the NNE, a trend close to MTDs deposited above this shale,
918 between Witmarsum and Aurora (Fig. 9). Palaeoslopes dipping to the W and SW
919 correspond well with a depocenter located in Santa Catarina state at that time (Rio do
920 Sul sub-basin), where isopachs of T3 (Rio do Sul-Taciba Formation) reach a
921 maximum. In this southern region, fluvial and delta-plain palaeocurrents developed
922 above the MTC are preferentially toward the W, with some variations to the SSW and
923 NW (Schemiko et al., 2019), whereas turbidity currents from below the MTC flowed
924 toward the NW with local variation to the SW (Fallgatter, 2015; Schemiko et al., 2019).
925 Therefore, MTDs with palaeoflow to SW and W are in agreement with fluvial/deltaic
926 palaeocurrent patterns, suggesting a close relationship between shoreline
927 progradation and subaqueous slope development (Fig. 10A, 10B, 10D and 10E).
928 However, MTD palaeoflows toward the N (NW and NE) may reflect local changes in
929 mass flow paths, which could be related to topographic control (Fig. 10F), but may also
930 have acted in a more regional way since this flow trend occurs in the northern portion
931 of the southern region (Fig. 9). Another aspect identified in this region is the similar
932 orientation between paleocurrents of fluvio-deltaic deposits and the palaeoflow of
933 slide/slump to blocky-flow MTDs (incipient to mature MTDs – DF-1 and DF-2; Fig. 9 –
934 localities 13, 15, 16, 17). Conversely, the palaeoflow of some blocky to debris-flow
935 MTDs (mature and evolved MTDs – DF-2 and DF-3; Fig. 9 – localities 10, 12, 14)
936 diverges from the fluvio-deltaic paleocurrents. Although the palaeoflows consist of local

indicators, these observations can be related to the runout aspect of mass-flows, where debris flows may show long runout distance (e.g., De Blasio and Elverhøi, 2011) and have their orientation controlled more by sea-floor topography or depocenter location rather than the palaeoslope azimuth (Fig. 10G; e.g., Gee et al., 1999; Bull et al., 2009; Alves and Cartwright, 2010). Even so, the variations in palaeoflow observed in the southern region may be related in some degree to different factors, including the limited degree of exposure, structural generation and modification during mass flow, radial spreading characteristics of MTDs, lateral/frontal confinement and local changes in the topography.

Location for Fig. 10 here.

5. Conclusions

Our study of deformational structures within MTDs of the Itararé Group has enabled us to evaluate their use in defining MTD palaeoflow in areas of limited exposure. In addition, we were able to define the local palaeoslope orientation for each locality, outline some implications for palaeogeography and enhance ongoing discussions about the evolution of the Paraná Basin during deposition of the Itararé Group. The following points highlight this in greater detail.

1) Through careful analysis of the geometry and orientation of deformational structures generated in gravity-induced mass flows (including coherent slide/slumps to debris flows), it is possible to define the orientation of the original palaeoslope. Limitations are related to outcrop exposure and palaeoflow variation within MTDs, which may be related to structural generation and modification during flow, lateral/frontal confinement and irregularities in slope and seafloow morphology. However, we consider the data from structures in

961 MTDs with limited exposure to indicate the orientation of the palaeoslope at a
962 local scale.
963 2) Field observations including structural geometry and a large number of
964 measurements are important to guarantee representativity of datasets,
965 particularly for MTDs with limited exposure. In many cases, the dataset
966 limitations related to number of data was compensated by preferential
967 orientation (usually related to structural geometry), and vice-versa. The
968 combination of statistical analysis of structural datasets, palaeoflow from each
969 kind of structure and each MTD outcrop palaeoflow allowed us to define data
970 reliability.
971 3) Fault and fold datasets from the same locality allow the azimuth of the
972 palaeoslope to be calculated with similar robustness. However, the complexity
973 of the data collected (folds and/or faults) related to the geometry and orientation
974 of the structure may affect the selection of appropriate methods of palaeoflow
975 definition and the robustness.
976 4) Beside faults and folds, the orientation data and/or kinematics of other
977 structures such as boudins, oriented intrabasinal and extrabasinal clasts, and
978 quarter structures may aid understanding of the flow and help define the
979 parental palaeoslope. For studies of MTDs with limited exposure, the sampling
980 of as many structures as possible may be essential to avoid ambiguous
981 interpretations sometimes provided by folds or faults alone. In mature MTDs
982 (DF3) or debris flows, other structures may be the only indicators of flow and
983 may display reasonably good robustness for defining palaeoslopes.
984 5) The analysis of MTD structures allows us to reliably define local palaeoslope
985 azimuths for different localities in different stratigraphic levels of the Itararé

Group. The MTD palaeoflows when combined with the palaeocurrents allows us to establish some general regional patterns for the palaeoslope in some regions. At the northern region studied, palaeoflow of T3 indicates a general orientation toward the SW. In the southern region, MTD palaeoflow ranges from SW to NNE from south to north across this region, with a general orientation toward the W. There is a depositional relationship between mass-transport deposits and progradational fluvio-deltaic systems identified in the southern region by Schemiko et al. (2019). Therefore, we can suggest that the MTD palaeoflow of this region tends to reflect the general azimuth of the palaeoslope, which corresponds to the progradational-aggradational clinoform system.

6) For palaeogeographic studies, it is recommended that several MTDs, at the same stratigraphic interval and region, are analysed regardless of exposure. Through the information gained from several MTDs, it is possible to more concisely define the main orientation of the original palaeoslope. In addition, some local variations in palaeoslope orientation and possible controls may be identified.

7) For the analysis of MTD kinematic indicators we suggest the term palaeoflow rather than palaeoslope. MTDs can be generated on the slope or gentle gradients on the seafloor and influenced by irregularities in the physiography. Thus, MTD palaeoflow should be discussed as the palaeoslope indicator. When compared to other kinds of data such as palaeocurrents of associated deposits, stratigraphical relationship with other deposits, isopach maps, tectonic structures, the palaeoslopes defined from MTDs palaeoflow can be identified as the palaeoslope and indicate irregularities in their morphologies. Therefore,

MTDs palaeoflow are a potential palaeomorphological and palaeogeographical tool.

Acknowledgments

This contribution is part of PhD research performed by the first author in the Postgraduate Program in Geology at UFPR with scholarship provided by Coordination for the Improvement of Higher Education Personnel (CAPES) Foundation. The study was funded by Brazilian National Council for Scientific and Technological Development (CNPq, grant 461650/2014–2, PQ 302842/2017-9 and PQ 306780/2019-4).

Data Availability

Datasets related to this article can be found at http://dx.doi.org/10.17632/hptsp9kyst.1, an open-source online data repository hosted at Mendeley Data.

References

Alfaro, E., Holz, M. 2014. Seismic geomorphological analysis of deepwater gravity-driven deposits on a slope system of the southern Colombian Caribbean margin. Mar. and Petr. Geo. 57, 294-311. https://doi.org/10.1016/j.marpetgeo.2014.06.002.

Allmendinger, R.W., Cardozo, N.C., Fisher, D., 2013. Structural geology algorithms: vectors and tensors. Cambridge, England, Cambridge University press, 289 p.

Alsop, G.I., Holdsworth, R.E., 1993. The distribution, geometry and kinematic significance of Caledonian buckle folds in the western Moine Nappe, northwest Scotland. Geological Magazine 130, 353-362.

Alsop, G.I., Holdsworth, R.E., 2007. Flow perturbation folding in shear zones. In: Ries, A.C., Butler, R.W.H., Graham, R.D. (Eds.), Deformation of the Continental Crust: The

1035 Legacy of Mike Coward. Geological Society, London, Special Publications 272, 77-
1036 103.
1037 Alsop, G.I., Marco, S., 2011. Soft-sediment deformation within seismogenic slumps of
1038 the Dead Sea Basin. J. Struct. Geol. https://doi.org/10.1016/j.jsg.2011.02.003
1039 Alsop, G.I., Marco, S., 2012. A large-scale radial pattern of seismogenic slumping
1040 towards the Dead Sea Basin. J. Geol. Soc. 169, 99–110. https://doi.org/10.1144/0016-
1041 76492011-032
1042 Alsop, G.I., Marco, S., 2013. Seismogenic slump folds formed by gravity-driven
1043 tectonics down a negligible subaqueous slope. Tectonophysics 605, 48–69.
1044 https://doi.org/10.1016/j.tecto.2013.04.004
1045 Alsop, G.I., Marco, S., 2014. Fold and fabric relationships in temporally and spatially
1046 evolving slump systems: A multi-cell flow model. J. Struct. Geol. 63, 27–49.
1047 https://doi.org/10.1016/j.jsg.2014.02.007
1048 Alsop, G.I., Marco, S., Weinberger, R., Levi, T., 2016. Sedimentary and structural
1049 controls on seismogenic slumping within mass transport deposits from the Dead Sea
1050 Basin. Sedim. Geol. 344, 71–90. https://doi.org/10.1016/j.sedgeo.2016.02.019
1051 Alsop, G.I., Marco, S., Weinberger, R., Levi, T., 2017. Upslope-verging back thrusts
1052 developed during downslope-directed slumping of Mass Transport Deposits. J. Struct.
1053 Geol. 100, 45-61.
1054 Alsop, G.I., Weinberger, R., Marco, S., Levi, T. 2019. Identifying soft-sediment
1055 deformation in rocks. *Journal of Structural Geology 125, 248-255.*

1056 Alsop, G.I., Weinberger, R., Marco, S., Levi, T., 2020. Distinguishing coeval patterns
1057 of contraction and collapse around flow lobes in mass transport deposits. J. Struct.
1058 Geol. 134, 104013. https://doi.org/10.1016/j.jsg.2020.104013

1059 Alsop, G.I., Weinberger, R. 2020. Are slump folds reliable indicators of downslope flow
1060 in recent mass transport deposits? J. Struct. Geol. 135, 104037.
1061 https://doi.org/10.1016/j.jsg.2020.104037
1062 Alves, T.M., 2015. Submarine slide blocks and associated soft-sediment deformation
1063 in deep-water basins: a review. Marine and Petroleum Geology.
1064 https://doi.org/10.1016/j.marpetgeo.2015.05.010
1065 Alves, T.M., Cartwright, J.A., 2009. Volume balance of a submarine landslide in the
1066 Espírito Santo Basin, offshore Brazil: quantifying seafloor erosion, sediment
1067 accumulation and depletion. Earth and Planet. Sci. Let. doi:10.1016/j.epsl.2009.10.020
1068 Alves, T.M., Cartwright, J.A., 2010. The effect of mass-transport deposits on the
1069 younger slope morphology, offshore Brazil. Mar. Petrol. Geol. 27, 2027–2036.
1070 https://doi.org/10.1016/j.marpetgeo.2010.05.006
1071 Amato, J.A., 2017. Using AMS to help interpret glaciogenic deposits of the Late
1072 Paleozoic Ice Age in the Paraná Basin, Brazil. Master degree thesis, The University of
1073 Wisconsin-Milwaukee, USA, 146p.
1074 Amerman, R., Nelson, E. P., Gardner, M. H., and Trudgill, B., 2011, Submarine mass-
1075 transport deposits of the Permian Cutoff Formation, west Texas, U.S.A.: Internal
1076 architecture and controls on overlying sand deposition, In: Shipp, R. C., Weimer, P.,
1077 and Posamentier, H. W., eds., Mass-Transport Deposits in Deepwater Settings, SEPM
1078 Special Publication 96: Tulsa, Oklahoma, SEPM (Society for Sedimentary Geology),
1079 p. 235–267.
1080 Armandita, C., Morley, C.K., Rowell, P., 2015. Origin, structural geometry, and the
1081 development of a giant slide: the South Makassar Strait mass transport complex.
1082 Geosphere 11, 376–403.

1083 Beraldin, S., 2014. Estratigrafia do Grupo Itararé na região de Balsa Nova (PR) e
1084 definição de critérios para sua distinção da Formação Furnas. Dissertação de
1085 Mestrado, Universidade Federal do Paraná, Brasil, 72p.
1086 Bull, S., Cartwright, J., Huuse, M., 2009. A review of kinematic indicators from mass-
1087 transport complexes using 3D seismic data. Mar. Petrol Geol. 26, 1132–1151.
1088 https://doi.org/10.1016/j.marpetgeo.2008.09.011
1089 Cardona, S., Wood L.J., Dugan, B., Jobe, Z., Strachan, L.J. 2020. Characterization of
1090 the Rapanui mass-transport deposit and the basal shear zone: Mount Messenger
1091 Formation, Taranaki Basin, New Zealand. Sedimentology 67, 2111-
1092 2148. https://doi.org/10.1111/sed.12697
1093 Cardozo, N., Allmendinger, R.W. 2013. Spherical projections with OSXStereonet.
1094 Computers & Geosciences 51, 193-205
1095 Carvalho, A.H., Vesely, F.F., 2017. Facies relationships recorded in a Late Paleozoic
1096 fluvio-deltaic system (Paraná Basin, Brazil): Insights into the timing and triggers of
1097 subaqueous sediment gravity flows. Sedim. Geol. 352, 45–62.
1098 https://doi.org/10.1016/j.sedgeo.2016.12.004
1099 Dalla-Valle, G., Gamberi, F., Foglini, F., Trincardi, F., 2015. The Gondola Slide: A mass
1100 transport complex controlled by margin topography (South-Western Adriatic Margin,
1101 Mediterranean Sea). Mar. Geol. 366, 97–113.
1102 https://doi.org/10.1016/j.margeo.2015.05.001
1103 Debacker, T.N., Sintubin, M., Verniers, J., 2001. Large-scale slumping deduced from
1104 structural and sedimentary features in the Lower Palaeozoic Anglo-Brabant fold belt,
1105 Belgium. J. Geol. Soc. of London 158, 341–352. https://doi.org/10.1144/jgs.158.2.341
1106 Debacker, T.N., Dumon, M., Matthys, A., 2009. Interpreting fold and fault geometries
1107 from within the lateral to oblique parts of slumps: A case study from the Anglo-Brabant

1108 Deformation Belt (Belgium). J. Struct. Geol. 31, 1525–1539.
1109 https://doi.org/10.1016/j.jsg.2009.09.002
1110 De Blasio, F.V., Elverhøi, A. 2011. Properties of Mass-Transport Deposits as Inferred
1111 from Dynamic Modeling of Subaqueous Mass Wasting: A Short Review. In: Shipp R.C.,
1112 Weimer, P., Posamentier, H.W. Mass-Transport Deposits in Deepwater Settings.
1113 https://doi.org/10.2110/sepmsp.096.499Elverhøi, A., Norem, H., Andersen, E.S.,
1114 Dowdeswell, J.A., Fossen, I., Haflidason H., Kenyon, N.H., Laberg, J.S., King, E.L.,
1115 Sejrup, H.P., Solheim, A., Vorren, T. 1997. On the origin and flow behavior of
1116 submarine slides on deep-sea fans along the Norwegian-Barents Sea continental
1117 margin. Geo-Mar. Lett., 17, 119–125.
1118 Fallgatter, C., 2015. Confined to unconfined deep-water systems of the Paraná (Brazil)
1119 and Paganzo (Argentina) basins. Tese de Doutorado (PhD thesis), UNISINOS, Brazil,
1120 191.
1121 Fallgatter, C., Paim, P.S.G., 2017. On the origin of the Itararé Group basal
1122 nonconformity and its implications for the Late Paleozoic glaciation in the Paraná
1123 Basin, Brazil. Palaeogeography, Palaeoclimatology, Palaeoecology.
1124 https://doi.org/10.1016/j.palaeo.2017.02.039
1125 Farrell, S.G., 1984. A dislocation model applied to slump stuctures, Ainsa Basin, south
1126 central Pyrenees. J. Struct. Geol. 6, 727–736.
1127 Farrell, S.G., Eaton, S. 1987. Slump strain in the Tertiary of Cyprus and the Spanish
1128 Pyrenees. Definition of palaeoslopes and models of soft sediment deformation. In:
1129 Jones M.F., Preston R.M.F. (Eds.), Deformation of Sediments and Sedimentary Rocks,
1130 Special Publication of the Geological Society of London, 29: 181-196.
1131 Fedorchuk, N.D., Isbell, J.L., Griffis, N.; Vesely, F.F., Rosa, E.L.M., Montanez, I.,
1132 Mundil, R., Yin, Q.Z., Iannuzzi, R., Roesler, G., Pauls, K. N. 2019. Carboniferous

1133 glaciotectonized sediments in the southernmost Paraná Basin, Brazil: Ice marginal
1134 dynamics and paleoclimate indicators. Sedimentary Geology 389, 54-
1135 72 . https://doi.org/10.1016/j.sedgeo.2019.05.006
1136 Festa, A., Dilek, Y., Codegone, G., Cavagna, S., Pini, G.A., 2013. Structural anatomy
1137 of the Ligurian accretionary wedge (Monferrato, NW Italy), and evolution of superposed
1138 mélanges. Geol. Soc. Amer. Bul., 125 (9–10): 1580–1598.
1139 Fleuty, M. J., 1964. The description of folds. Proc. Geol. Assoc., 75, 461-492.
1140 Fossen, H., 2016. Structural geology. Cambridge University Press, 2nd edition, 510p.
1141 França, A.B., Potter, P.E., 1988. Estratigrafia, ambiente deposicional e análise de
1142 reservatório do Grupo Itararé (Permocarbonífero), Bacia do Paraná (parte 1). Bol.
1143 Geoc. Petrobrás, 2: 147-191.
1144 França, A.B., Potter, P.E. 1991. Stratigraphy and reservoir potential of glacial deposits
1145 of the Itararé Group (Carboniferous-Permian), Paraná Basin, Brazil. AAPG Bulletin,
1146 75: 62-85.
1147 Gee, M.J.R., Masson, D.G., Watts, A.B., Allen, P.A., 1999. The Saharan debris flow:
1148 An insight into the mechanics of long runout submarine debris flows. Sedimentology
1149 46, 317–335. https://doi.org/10.1046/j.1365-3091.1999.00215.x
1150 Goscombe, B.D., Passchier, C.W., Hand, M., 2004. Boudinage classification: End-
1151 member boudin types and modified boudin structures. J. Struct. Geol. 26, 739–763.
1152 https://doi.org/10.1016/j.jsg.2003.08.015
1153 Hansen, E., 1971. Strain Facies. Springer-Verlag, Berlin, 207p.
1154 Holdsworth, R.E., 1988. The stereographic analysis of facing. J. Struct. Geol. 10, 219–
1155 223. https://doi.org/10.1016/0191-8141(88)90119-8
1156 Holdsworth, R.E., 1990. Progressive deformation structures associated with ductile
1157 thrusts in the Moine Nappe, Sutherland, N. Scotland. J. Struct. Geol., 12: 443-452.

1158 Holz, M., França, A.B., Souza, P.A., Iannuzzi, R., Rohn, R., 2010. A stratigraphic chart
1159 of the Late Carboniferous/Permian succession of the eastern border of the Paraná
1160 Basin, Brazil, South America. J. South Amer. Earth Sci. 29, 381–399.
1161 https://doi.org/10.1016/j.jsames.2009.04.004
1162 Jablonská, D., Di Celma, C., Korneva, I., Tondi, E., Alsop, I., 2016. Mass-Transport
1163 deposits within basinal carbonates from southern Italy. Italian J. Geosc. 135, 30–40.
1164 https://doi.org/10.3301/IJG.2014.51
1165 Jablonská, D., Di Celma, C.N., Alsop, G.I., Tondi, E., 2018. Internal architecture of
1166 mass-transport deposits in basinal carbonates: A case study from southern Italy.
1167 Sedimentology 65, 1246–1276. https://doi.org/10.1111/sed.12420
1168 Jones, O.T. 1939. The geology of the Colwyn Bay district: A study of submarine
1169 slumping during the Salopian period: Geological Society of London Quarterly Journal,
1170 95: 335–382.
1171 Juk, K.F.V., 2016. Reservatórios turbidíticos e depósitos de transporte em massa
1172 associados a progradações deltaicas: estudo comparativo integrando dados de
1173 subsuperfície e afloramentos. Dissertação de mestrado. Universidade Federal do
1174 Paraná, Brasil, 76p.
1175 Lewis, K.B., 1971. Slumping on a continental slope inclined at 1–4°. Sedimentology,
1176 16: 97–110.
1177 Maltman, A., 1984. On the term “soft-sediment deformation.” J. Struct. Geol. 6, 589–
1178 592. https://doi.org/10.1016/0191-8141(84)90069-5
1179 Maltman, A., 1994a. The Geological Deformation of Sediments. Chapman & Hall,
1180 London, 362 p.
1181 Maltman, A., 1994b. Introduction and overview. In: Maltman, A. (Ed.), The Geological
1182 Deformation of Sediments. Chapman & Hall, London, p. 1-35.

1183 Martinsen, O.J., 1989. Styles of soft-sediment deformation on a Namurian
1184 (Carboniferous) delta slope, Western Irish Namurian Basin, Ireland. Geological
1185 Society, London, Special Publications 41, 167–177.
1186 https://doi.org/10.1144/GSL.SP.1989.041.01.13
1187 Martinsen, O.J., 1994. Mass movements. In: Maltman, A., ed., The Geological
1188 Deformation of Sediments: London, Chapman & Hall, 127–165.
1189 Middleton, G.V., Hampton, M.A. 1976. Subaqueous sediment transport and deposition
1190 by sediment gravity flows. In: Stanley, D.J., Swift, D.J.P. Marine Sediment Transport
1191 and Environmental Management, Wiley, New York, 197–218.
1192 Mottin, T.E., Vesely, F.F., de Lima Rodrigues, M.C.N., Kipper, F., de Souza, P.A.,
1193 2018. The paths and timing of late Paleozoic ice revisited: New stratigraphic and paleo-
1194 ice flow interpretations from a glacial succession in the upper Itararé Group (Paraná
1195 Basin, Brazil). Palaeogeography, Palaeoclimatology, Palaeoecology 490, 488–504.
1196 https://doi.org/10.1016/j.palaeo.2017.11.031
1197 Naji, C., Gharbi, M., Amri, Z., Masrouhi, A., Bellier, O., 2018. Temporal and spatial
1198 changes of the submarine Cretaceous paleoslope in Northern Tunisia, inferred from
1199 slump folds analysis. Proceedings of the Geologists' Association 129, 40–56.
1200 Ogata, K., Festa, A., Pini, G.A., Alonso, J.L. 2019. Submarine Landslide Deposits in
1201 Orogenic Belts. In: Ogata, K., Festa, A., Pini, G.A. Submarine Landslides: Subaqueous
1202 Mass Transport Deposits from Outcrops to Seismic Profiles. Geophysical Monograph
1203 Series, American Geophysical Union. https://doi.org/10.1002/9781119500513.ch1
1204 Ogata, K., Mutti, E., Pini, G.A., Tinterri, R., 2012a. Mass transport-related stratal
1205 disruption within sedimentary mélanges: Examples from the northern Apennines (Italy)
1206 and south-central Pyrenees (Spain). Tectonophysics 568–569, 185–199.
1207 https://doi.org/10.1016/j.tecto.2011.08.021

1208 Ogata, K., Tinterri, R., Pini, G.A., Mutti, E., 2012b. The Specchio Unit (Northern
1209 Apennines, Italy): an ancient mass transport complex originated from near coastal
1210 areas in an intra-slope setting. In: Yamada, Y., Kawamura, K., Ikehara, K., Ogawa, Y.,
1211 Urgeles, R., Mosher, D., Chaytor, J., Strasser, M., (eds) Submarine mass movements
1212 and their consequences. advances in natural and technological hazards research.
1213 Springer, Netherlands, 595–605.
1214 Ogata, K., Pini, G.A., Festa, A., Pogacˇnik, Z., Tunis, G., 2014a. High-Resolution
1215 Studies of Mass Transport Deposits: Outcrop Perspective for Understanding
1216 Modern Submarine Slope Failure and Associated Natural Hazards. In: Lollino G.,
1217 Manconi A., Locat J., Huang Y., Canals Artigas M. (eds) Engineering Geology for
1218 Society and Territory – Volume 4. Springer, Cham. https://doi.org/10.1007/978-3-
1219 319-08660-6_40
1220 Ogata, K., Pogacˇnik, Z., Pini, G.A., Tunis, G., Festa, A., Camerlenghi, A., Rebesco,
1221 M., 2014b. The carbonate mass transport deposits of the Paleogene Friuli Basin
1222 (Italy/Slovenia): Internal anatomy and inferred genetic processes. Mar. Geol. 356, 88–
1223 110. https://doi.org/10.1016/j.margeo.2014.06.014
1224 Ogata, K., Pini, G. A., Festa, A., Pogacnik, Z., Lucente, C. C., 2016. Meso-Scale
1225 Kinematic Indicators in Exhumed Mass Transport Deposits: Definitions and
1226 Implications. IN: G. Lamarche et al. (eds.), Submarine Mass Movements and their
1227 Consequences, Advances in Natural and Technological Hazards Research 41, DOI
1228 10.1007/978-3-319-20979-1_46Passchier, C.W., Trouw, R.A., 2005. Microtectonics.
1229 Springer, Berlin.
1230 Posamentier, H.W., Martinsen, O.J., 2011. The character and genesis of submarine
1231 mass-transport deposits; insights from outcrop and 3D seismic data, Mass-Transport
1232 Deposits in Deepwater Settings. SEPM Special Publication 96, 7–38.

1233 Ramsay, J. G., 1967. Folding and Fracturing of Rocks. New York, McGraw Hill, 568p.
1234 Rodrigues, M. C. N. L., Trzaskos, B., Alsop, G. I., Vesely, F.F. 2020. Making a
1235 homogenite: An outcrop perspective into the evolution of deformation within mass-
1236 transport deposits. Mar. Petrol. Geol., 112 104033.
1237 https://doi.org/10.1016/j.marpetgeo.2019.104033
1238 Rosa, E.L.M., Vesely, F.F., Isbell, J., Kipper, F., Fedorchuk, N., Souza, P.A., 2019
1239 Constraining the timing, kinematics and cyclicity of Mississippian-early Pennsylvanian
1240 glaciations in the Paraná Basin, Brazil. Sedim. Geol., 384, 29-49.
1241 Rostirolla, S.P., Mancini, F., Rigoti, A., Kraft, R.P., 2003. Structural styles of the
1242 intracratonic reactivation of the Perimbó fault zone, Paraná basin, Brazil. J. South
1243 Amer. Earth Sci. 16, 287–300. https://doi.org/10.1016/S0895-9811(03)00065-8
1244 Schemiko, D.C.B., Vesely, F.F., Rodrigues, M.C.N.L., 2019. Deepwater to fluvio-
1245 deltaic stratigraphic evolution of a deglaciated depocenter: The early Permian Rio do
1246 Sul and Rio Bonito formations, southern Brazil. J. South Amer. Earth Sci. 95, 102260
1247 https://doi.org/10.1016/j.jsames.2019.102260
1248 Schneider, R. L., Muhlmann, H., Tommasi, E., Medeiros, R.A., Daemon, R.A.,
1249 Nogueira, A.A., 1974. Revisão estratigráfica da Bacia do Paraná. In: SBG, 28
1250 Congresso Brasileiro de Geologia, Porto Alegre, 1, 41-65.
1251 Sharman, G.R., Graham, S.A., Masalimova, L.U., Shumaker, L.E., King, P.R., 2015.
1252 Spatial patterns of deformation and paleoslope estimation within the marginal and
1253 central portions of a basin-floor mass-transport deposit, Taranaki Basin, New Zealand.
1254 Geosphere 11, 266–306. https://doi.org/10.1130/GES01126.1
1255 Sobiesiak, M.S., Kneller, B., Alsop, G.I., Milana, J.P., 2016. Internal deformation and
1256 kinematic indicators within a tripartite mass transport deposit, NW Argentina. Sedim.
1257 Geol. 344, 364–381. https://doi.org/10.1016/j.sedgeo.2016.04.006

1258 Sobiesiak, M., Kneller, B.C., Alsop, G.I., Milana, J.P. 2017. Sub-seismic scale folding
1259 and thrusting within an exposed mass transport deposit: A case study from NW
1260 Argentina. J. Struct. Geol. 96, 176-191. https://doi.org/10.1016/j.jsg.2017.01.006
1261 Sobiesiak, M.S., Kneller, B., Alsop, G.I., Milana, J.P. 2018. Styles of basal interaction
1262 beneath mass transport deposits. Mar. Petrol. Geol., 98, 629–639.
1263 Souza, P.A., 2006. Late Carboniferous palynostratigraphy of the Itararé Subgroup,
1264 northeastern Paraná Basin, Brazil. Review of Palaeobotany and Palynology: 138, 9–
1265 29.
1266 Strachan, L.J., 2002. Slump-initiated and controlled syndepositional sandstone
1267 remobilization; an example from the Namurian of County Clare, Ireland.
1268 Sedimentology, 49: 25-41.
1269 Strachan, L.J. 2008. Flow transformations in slumps: a case study from the Waitemata
1270 Basin, New Zealand. Sedimentology, 55, 1311–1332.
1271 Strachan, L.J., Alsop, G.I., 2006. Slump folds as estimators of palaeoslope: A case
1272 study from the Fisherstreet Slump of County Clare, Ireland. Basin Research 18, 451–
1273 470. https://doi.org/10.1111/j.1365-2117.2006.00302.x
1274 Suss, J.F., Vesely, F.F., Santa Catharina, A., Assine, M.L., Paim, P.S.G., 2014. O
1275 grupo itararé (Neocarbonífero-eopermiano) entre Porto Amazonas (PR) e Mafra (SC):
1276 Sedimentação gravitacional em contexto marinho deltaico com influência glacial.
1277 Geociencias 33, 701–719.
1278 Trzaskos, B., Vesely, F.P., Rostirolla, S.P., 2006. Eventos tectônicos recurrentes
1279 impressos no arcabouço estratigráfico do Grupo Itararé na região de Vila Velha,
1280 Estado do Paraná. Bol. Paran. Geoc., 89–104.
1281 Twiss, R.J., Moores, E.M., 2007. Structural Geology. University of California at Davis.
1282 2ª edição, W. H. Freeman and Company, Nova Iorque, 736p.

1283 Vesely, F.F., 2006. Dinâmica sedimentar e arquitetura estratigráfica do Grupo Itararé
1284 (Carbonífero-Permiano) no centro-leste da Bacia do Paraná. PhD thesis. Universidade
1285 Federal do Paraná, Brasil, 226p.
1286 Vesely, F.F., Assine, M.L., 2006. Deglaciation sequences in the Permo-Carboniferous
1287 Itararé Group, Paraná Basin, southern Brazil. J. South Amer. Earth Sci. 22, 156–168.
1288 https://doi.org/10.1016/j.jsames.2006.09.006
1289 Woodcock, N.H., 1976a. Ludlow Series slumps and turbidites and the form of the
1290 Montgomery Trough, Powys, Wales. Proceedings of the Geologists' Association, 87,
1291 169–182.
1292 Woodcock, N.H., 1976b. Structural style in slump sheets: Ludlow Series, Powys,
1293 Wales. Journal of the Geological Society, London, 132, 399–415.
1294 Woodcock, N.H., 1977. Specification of fabric shapes using an eigenvalue method
1295 Geological Society of America Bulletin 88: 1231-1236.
1296 Woodcock, N.H., 1979. The use of slump structures as palaeoslope orientation
1297 estimators. Sedimentology 26: 83–99. https://doi.org/10.1111/j.1365-
1298 3091.1979.tb00339.x
1299 Woodcock N.H., Naylor M.A., 1983. Randomness testing in three-dimensional
1300 orientation data. J. Struct. Geol. 5 (5): 539-548
1301
1302 Fig. 1: Location map and stratigraphic setting of the study area in the Paraná Basin of
1303 southern Brazil (Modified from Rodrigues et al. 2020). The geographic location,
1304 stratigraphic position and type of deformation facies of each examined mass-transport
1305 deposit are indicated by numbers and symbols respectively.
1306

Fig. 2: Different types of structures associated with mass movements. A) Open and asymmetrical fold (Locality 1). B) Closed and asymmetrical fold (Locality 11). C) Diapiric folds with preferential vergence resulting from loading of sandstone over rhythmite combined with shearing (Locality 3; modified from Vesely, 2006). D) Reverse fault with associated drag fold (Locality 12). E) Normal faults (Locality 17). F) Displacement surface with slickenlines in continuous clay smear (Locality 8). G) Clay-sand smear with SC-like feature (Locality 9). H) Reverse anastomosed fault zone (Locality 12). I) Sandy injectites in the form of sills and dikes (Locality 1). J) Asymmetric boudins (Locality 10). K) Oriented sandstone clasts (Locality 14). L) Grooves/scratch marks at the margin of intrabasinal clasts (Locality 6). M) Quarter structure around a granite clast (Locality 10). N) Heterogeneous matrix with discrete textural/compositional banding (banded matrix; Locality 8). Photographs B, C and E represent incipient MTDs (DF-1); photographs A, I, J and M are examples of mature MTDs (DF-2); and photographs D, F, G, H, K, L and N correspond to evolved MTDs (DF-3). Refer to Fig. 1 for locations.

Fig. 3: Example of fold sets studied with stereograms and graphs (axial planar dip angle versus interlimb angle), with indication of transport direction (shown in the stereograms by arrows) obtained through each applied method (as indicated by acronyms): A) Gentle and symmetrical folds generated by LPS (locality 17); B) Asymmetrical folds generated by LPS with positive relationship between axial planar dip and interlimb angle indicating possible progressive deformation (locality 13); C) Asymmetrical folds generated by LNS with relatively positive relationship between axial planar dip and interlimb angle indicating possible progressive deformation (locality 1); and D) Recumbent folds, with close interlimb angle, generated by LNS (locality 11). E)

Diapiric folds that show a positive relationship between axial planar dip and interlimb angle indicating progressive deformation (locality 3). The number of data (N) is indicated next to each stereogram. Histograms of all fold datasets: F) indicating the confidence interval (95%) of fold elements (hinge, axial plane and facing); and G) indicating the confidence interval (95%) of the average transport direction of each fold dataset (each locality). For some fold datasets it was not possible to obtain confidence intervals (95%) due to limited number of measurements: 23% of hinges, 22.2% of axial planes and 11.1% of facing; and 21.4% of folds average transport direction.

Fig. 4: Example of fault datasets stereograms: A) Normal faults with single cluster (locality 17), possible antithetic faults (with respect to regional information from palaeocurrents of adjacent deposits) associated with major normal fault; B) Normal faults with conjugate parallel patterns (locality 10), in which the main cluster was identified as the synthetic faults with respect to other kinematic indicators; C) Normal faults with conjugate oblique patterns (locality 16); D) Normal, reverse and unidentified faults that show more or less parallel strike, while normal and reverse faults show opposing dip directions that indicate flow toward the NE (locality 9); E) Normal, reverse and unidentified faults, of which normal and reverse faults show parallel strike and opposing dip directions indicating flow toward the NE (locality 12); F) Reverse fault and faults of unidentified kinematics (some intrastratal) with slickenlines (locality 4). Histograms of all fault datasets: G) indicating the confidence interval (95%) of faults and slickenlines; and H) indicating the confidence interval (95%) of the average transport direction of each fault dataset (each locality) from transport directions obtained through different methods of palaeoslope definition (indicated in the stereograms by arrows and method by acronym). For some fault datasets it was not

possible to obtain confidence intervals (95%) due to limited number of measurements: 9.5% of fault datasets; and 6.7% of fault average transport directions. I) Histogram of angle between the orientation of average transport directions of faults and folds from the same locality (N = 13) with indication of the range of variation. The number of data (N) is indicated next to each stereogram.

Fig. 5: Stereograms of injectite datasets: A) Injectites associated with continuous clay smear and normal kinematics (locality 8); B) Dikes and associated sills (locality 13); C) Sill and associated thicker dikes (I) generated in a first stage and thinner dikes (II) generated during a second stage (locality 1). The number of data (N) is indicated next to each stereogram. Histograms of injectite datasets: D) indicating the confidence interval (95%) of injectite clusters; and E) indicating the confidence interval (95%) of the average transport direction of injectite datasets of each locality from transport directions obtained by comparison with other structures (indicated in the stereograms by arrows).

Fig. 6: Histograms of: A) the angle between the transport direction of bedding and banded matrix with the transport direction calculated from structures; B) the angle between the final transport direction of each locality with and without the transport direction of bedding and banded matrix (MBSM); C) the confidence interval (95%) of datasets of bedding and banded matrix; D) the confidence interval (95%) of the final transport direction of each locality without MBSM - for 11.1% of cases no confidence interval (95%) was obtained due to the limited number of measurements (corresponding to locality 15); and E) the confidence interval (95%) of the final transport direction of each locality with MBSM.

Fig. 7: A) Stereogram of asymmetric boudins with boudin faults and axes plotted and transport directions (indicated in the stereograms by arrows) calculated from different methods of palaeoslope analysis (indicated by acronyms; locality 10). B) Rose diagram of slickenlines of intrastratal detachment surfaces with transport direction (indicated in the stereograms by arrows; locality 10). C) Rose diagram of oriented extrabasinal clasts with transport direction (indicated in the stereograms by arrows; locality 14). D) Rose diagram of oriented intrabasinal clasts with transport direction (indicated in the stereograms by arrows; locality 14), E) Rose diagram of grooves and scratch marks at intrabasinal clasts with transport direction (indicated in the stereograms by arrows; locality 6). The number of data (N) is indicated next to each stereogram or rose diagram. F) Graph with the confidence intervals (95%) of each element of asymmetric boudins (faults and axis) and the average transport direction of asymmetric boudins, as well as, the confidence interval of the datasets of oriented intrabasinal and extrabasinal clasts, grooves/scratch marks and intrastratal slickenlines.

Fig. 8: A) Angle between the palaeoflows obtained from each structure from the same outcrop. B) Histogram of the confidence interval of palaeoflows from the studied MTDs (N = 16) with indication of range of variation.

Fig. 9: Maps displaying the palaeoflow of studied MTDs, in each stratigraphic level (T1 to T3) that correspond with the azimuth of the local palaeoslope, together with indications of confidence intervals. NM is the number of methods applied. The palaeoflow of locality 7 shows none robustness and confidence interval, because it was inferred from kinematic indicators, such as asymmetric folds and sigma structures,

with the structures being inaccessible for measurements. The maps also highlight the palaeocurrents of fluvial deltaic deposits and turbidites described in several studies (e.g. Vesely and Assine, 2006; Beraldin, 2014; Suss et al., 2014; Juk, 2016; Amato, 2017; Carvalho and Vesely, 2017; Fallgatter and Paim, 2017; Mottin et al., 2018; Schemiko et al., 2019; Rosa et al., 2019).

Fig. 10: Schematic block diagram that illustrates some of the possible orientations of MTD palaeoflow with respect to the main orientation of the parental palaeoslope and the depocenter. In addition, some possible morphological controls in the palaeoslope and seafloor are also shown. A) and B) Incipient and mature MTDs (DF-1 to DF-2 – slide/slump to blocky-flows), respectively, with general palaeoflow parallel to the main palaeoslope orientation. C) Incipient to mature MTD (DF-1 to DF-2 – slide/slump to blocky-flows), with palaeoflow oblique to main palaeoslope orientation. D) and E) Incipient to mature MTD and evolved MTD (DF-1 to DF-3 – slide/slump to debris flows), respectively, with general palaeoflow parallel to the main palaeoslope orientation. F) Incipient to evolved MTD (DF-1 to DF-3 – slide/slump to debris flows) with proximal palaeoflow orientation parallel to the main palaeoslope orientation, and the distal portion reoriented by a structural high. G) Mature to evolved MTD (DF-2 to DF-3 – slump to debris flows) with proximal palaeoflow parallel to the main palaeoslope orientation and the distal portion reoriented toward the basin depocenter. H) Incipient to mature MTD (DF-1 to DF-2 – slide/slump to blocky-flows) developed on a slope related to a morphological irregularity in the seafloor. F.D.D. are fluvial-deltaic deposits; S.D. are slope deposits; and, D.M.D. are deep-marine deposits.

Table 1: Deformational facies based on matrix proportion, intrabasinal clasts and deformation structures identified in the localities studied.

Table 2: Summary of methods used to define palaeoslope orientations.

Table 3: Structural datasets of preferred fold orientations based on Strength parameter C and datasets, transport direction and general classification based on different parameters indicated in Appendices A and B.

Table 4: Confidence interval (95%) of structural datasets and transport direction defined by methods applied to each structure.

Table 5: Evaluation of bedding and banded matrix with respect to transport direction defined from structures and final transport direction of each MTD.

Appendix A

Table with evaluation of structural datasets from each outcrop locality studied (O). Parameters analysed: number of data measured (N.d.); strength parameter C and respective preferential orientation (P.o.); and confidence interval of 95% (c.i. ±; in degrees). For each parameter, a classification value (c.v.) was given from which an average classification value (c.v.') was obtained by dataset. For each outcrop structure, a classification value (S.D. – Structural dataset classification) from all datasets of the same structure was obtained. From all S.D. of a locality, the outcrop classification (O.C.) was defined, which was used in the final classification. Average classification value (c.v.') by dataset, structural dataset classification (S.D.) and outcrop classification (O.C.) were obtained through mode or mean (where no clear

mode existed) of classification values for the cited parameters or classification values. Number of measurements and respective c.v.: N.d. ≤ 5 = 1; 5<N.d.≥10 = 2; 10<N.d.≥20 = 3; 20<N.d.≥30 = 4; 30<N.d.≥40 = 5; N.d. > 40 = 6. P.o. and respective c.v.: none = 1; weak = 2; moderate = 3; and strong = 4. Classification value for confidence interval (95%): c.i. ≤ 10° is 5; 10º< c.i. ≥20° is 4; 20°< c.i. ≥30° is 3; 30°< c.i. ≥40° is 2; and c.i. >40° is 1. The degrees of robustness consist of: a) no robustness (cv = 0); b) very weak robustness (cv = 1); c) weak robustness (cv = 2); d) moderate robustness (cv = 3); e) strong robustness (cv = 4); f) very strong robustness (cv ≥ 5).

Appendix A table here.

Appendix B

Table with evaluation of structural transport direction and final transport direction from each outcrop locality studied (O). Parameters analysed: number of methods (N.M.) and confidence interval of 95% (c.i. ±; in degrees). The number of methods here was considered as a classification value and for c.i. was given a classification value (c.v.). From these parameters of structural transport direction and the dataset classification value (S.D.) an average classification value (c.v.') was obtained by dataset. For each outcrop structure a classification value (c.v.") from all datasets c.v.' of the same structure was obtained. From all c.v." of a locality an outcrop classification value (O.C.'), which was used in the final classification was defined. From the c.v. of number of methods applied in each outcrop and c.i. (95%) of the final transport direction an outcrop classification (O.C") was defined. The final classification (F.C.) considers structural dataset classification (O.C. in Appendix A), structural transport direction classification (O.C.') in the structural transport direction section) and final transport direction classification (O.C." in the final transport direction section). The classification value for confidence interval (95%) is the same applied in Appendix A. Each outcrop

structure classification value (c.v.”), outcrop classification value (O.C.’), final transport direction classification (O.C.”) and final classification (F.C.) were obtained through mode or mean (where no clear mode existed) of classification values for the cited parameters or classification values. The classification value for all methods applied in each outcrop (N.M.’) is: c.v. = 1 for 1 method; c.v. = 2 for 2 to 3 methods; c.v. = 3 for 4 to 6 methods; c.v. = 4 for 7 to 10 methods; and c.v. = 5 for more than 10 methods. The degrees of robustness consist of: a) no robustness (cv = 0); b) very weak robustness (cv = 1); c) weak robustness (cv = 2); d) moderate robustness (cv = 3); e) strong robustness (cv = 4); f) very strong robustness (cv ≥ 5).

Appendix B table here.

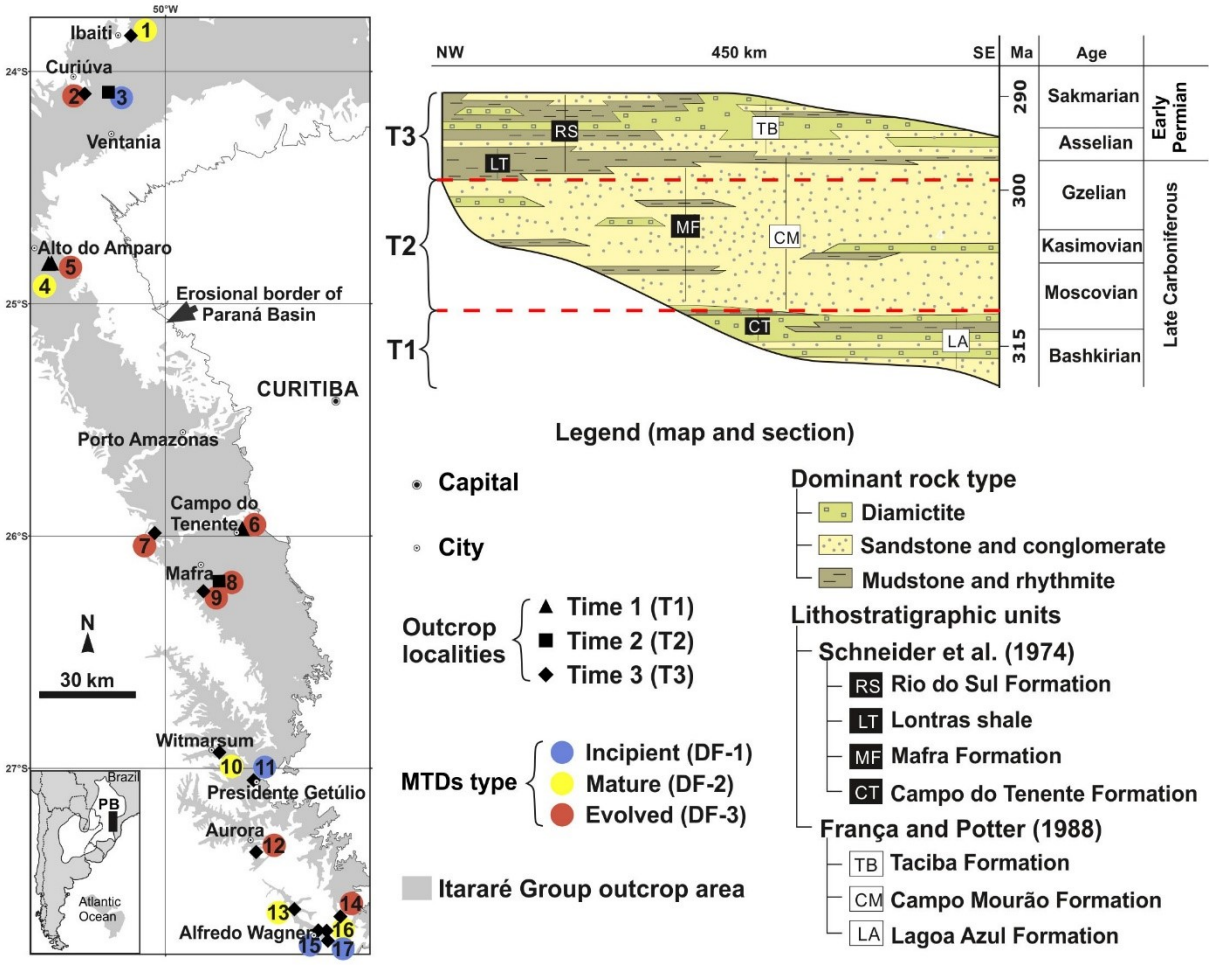
50°W
24°S
25°S
26°S
27°S
Ibaiti
Curiúva
Ventania
Alto do Amparo
Erosional border of Paraná Basin
CURITIBA
Porto Amazonas
Campo do Tenente
Mafra
N
30 km
Witmarsum
Presidente Getúlio
Aurora
Alfredo Wagner
Brazil
PB
Atlantic Ocean
NW
450 km
SE
Ma
Age
T3
T2
T1
RS
TB
LT
MF
CM
CT
LA
290
300
315
Sakmarian
Asselian
Gzelian
Kasimovian
Moscovian
Bashkirian
Early Permian
Late Carboniferous
Legend (map and section)
Capital
City
Outcrop localities
Time 1 (T1)
Time 2 (T2)
Time 3 (T3)
MTDs type
Incipient (DF-1)
Mature (DF-2)
Evolved (DF-3)
Itararé Group outcrop area
Dominant rock type
Diamictite
Sandstone and conglomerate
Mudstone and rhythmite
Lithostratigraphic units
Schneider et al. (1974)
RS Rio do Sul Formation
LT Lontras shale
MF Mafra Formation
CT Campo do Tenente Formation
França and Potter (1988)
TB Taciba Formation
CM Campo Mourão Formation
LA Lagoa Azul Formation

1493

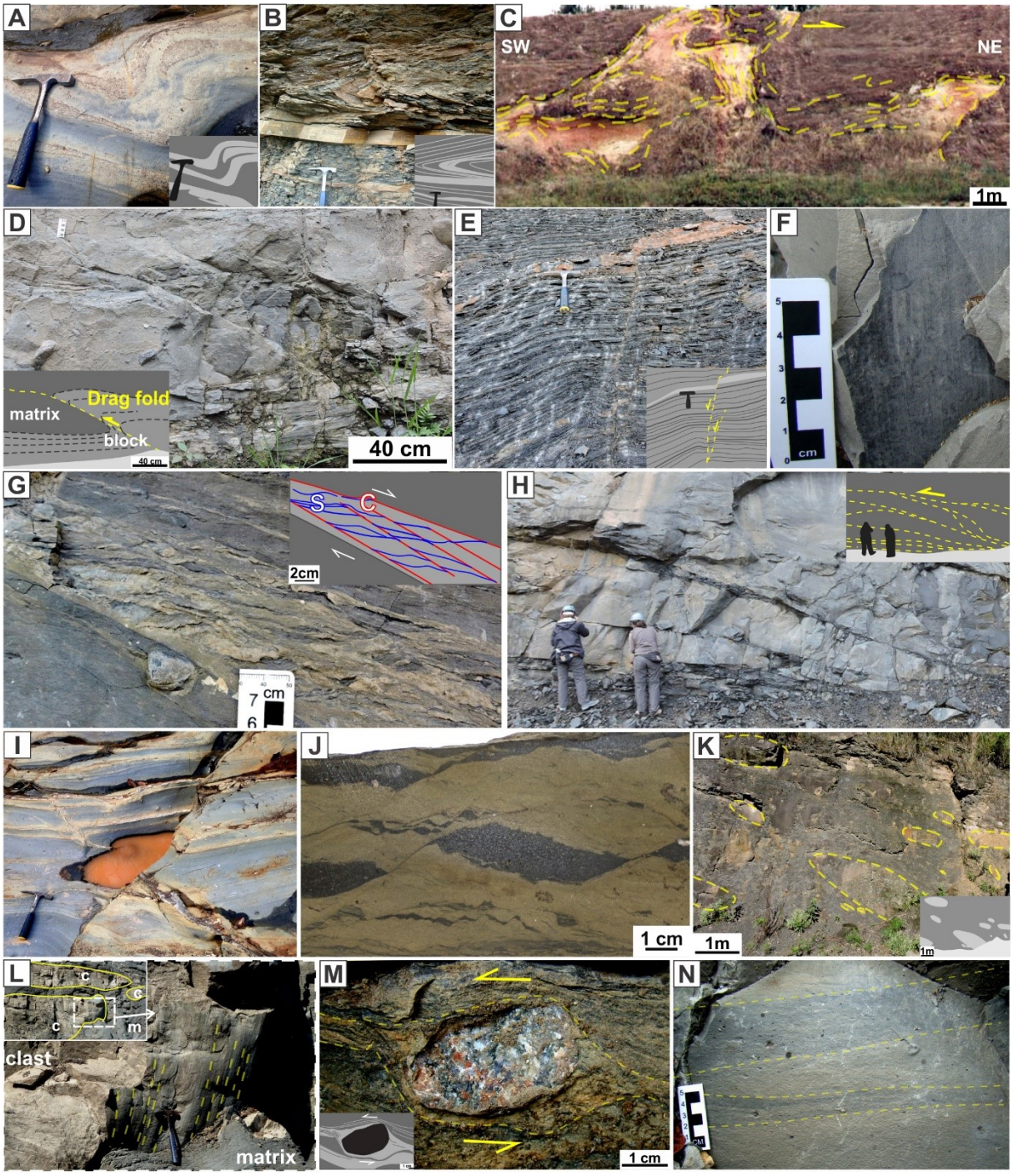
A
B
C
SW
NE
1m
D
Drag fold
matrix
block
40 cm
E
F
cm
G
S
C
2cm
7 cm
H
I
J
1 cm
K
1m
L
clast
matrix
M
1 cm
N

1494

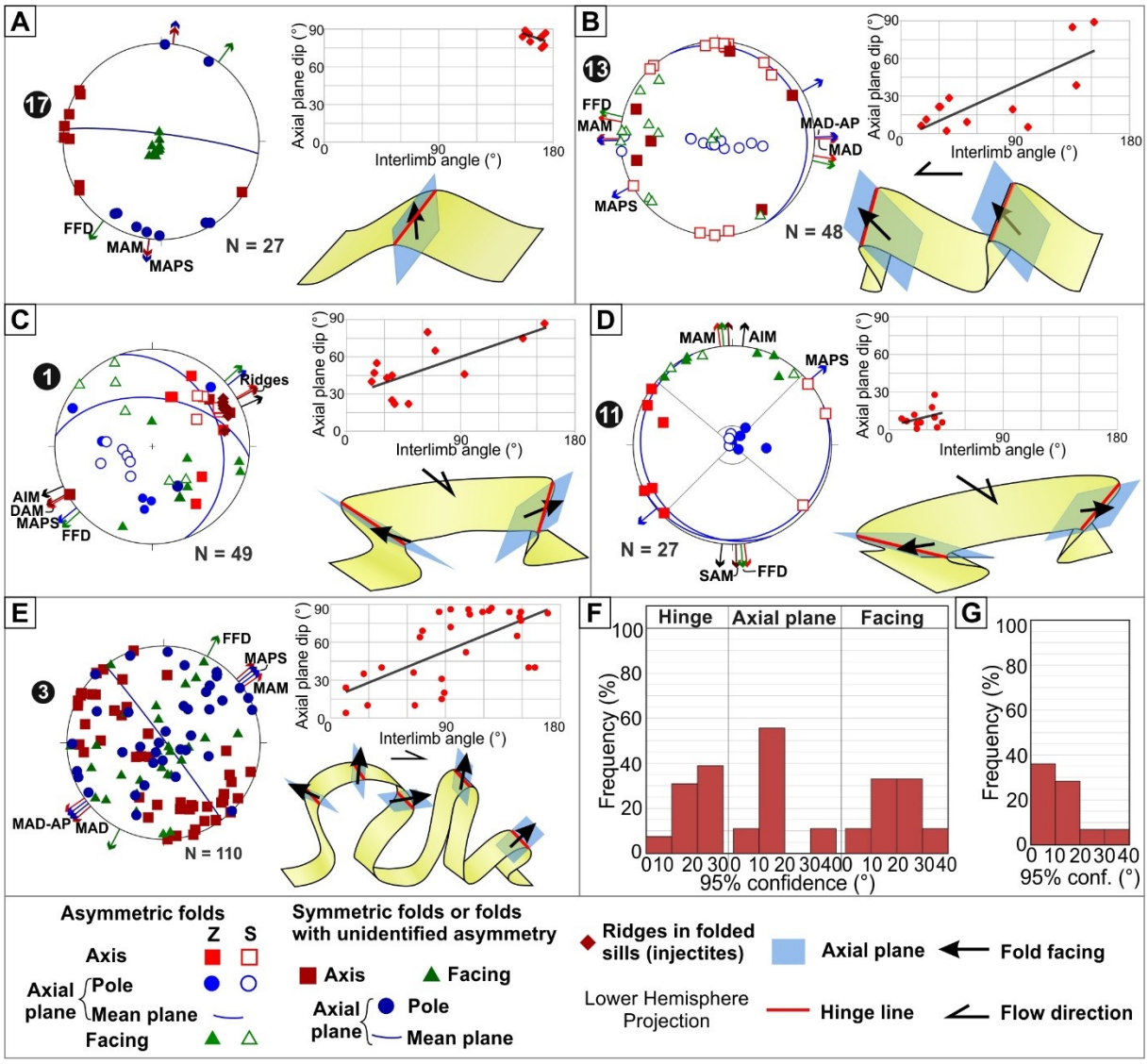
A
17
FFD
MAM
MAPS
N = 27
Axial plane dip (°)
Interlimb angle (°)
B
13
FFD
MAM
MAPS
MAD-AP
MAD
N = 48
C
1
Ridges
AIM
DAM
MAPS
FFD
N = 49
D
11
MAM
AIM
MAPS
N = 27
SAM
FFD
E
3
FFD
MAPS
MAM
MAD-AP
MAD
N = 110
F
Hinge
Axial plane
Facing
Frequency (%)
95% confidence (°)
G
Frequency (%)
95% conf. (°)
Asymmetric folds
Z S
Axis
Axial plane
Pole
Mean plane
Facing
Symmetric folds or folds with unidentified asymmetry
Axis
Facing
Axial plane
Pole
Mean plane
Ridges in folded sills (injectites)
Axial plane
Fold facing
Lower Hemisphere Projection
Hinge line
Flow direction

1495

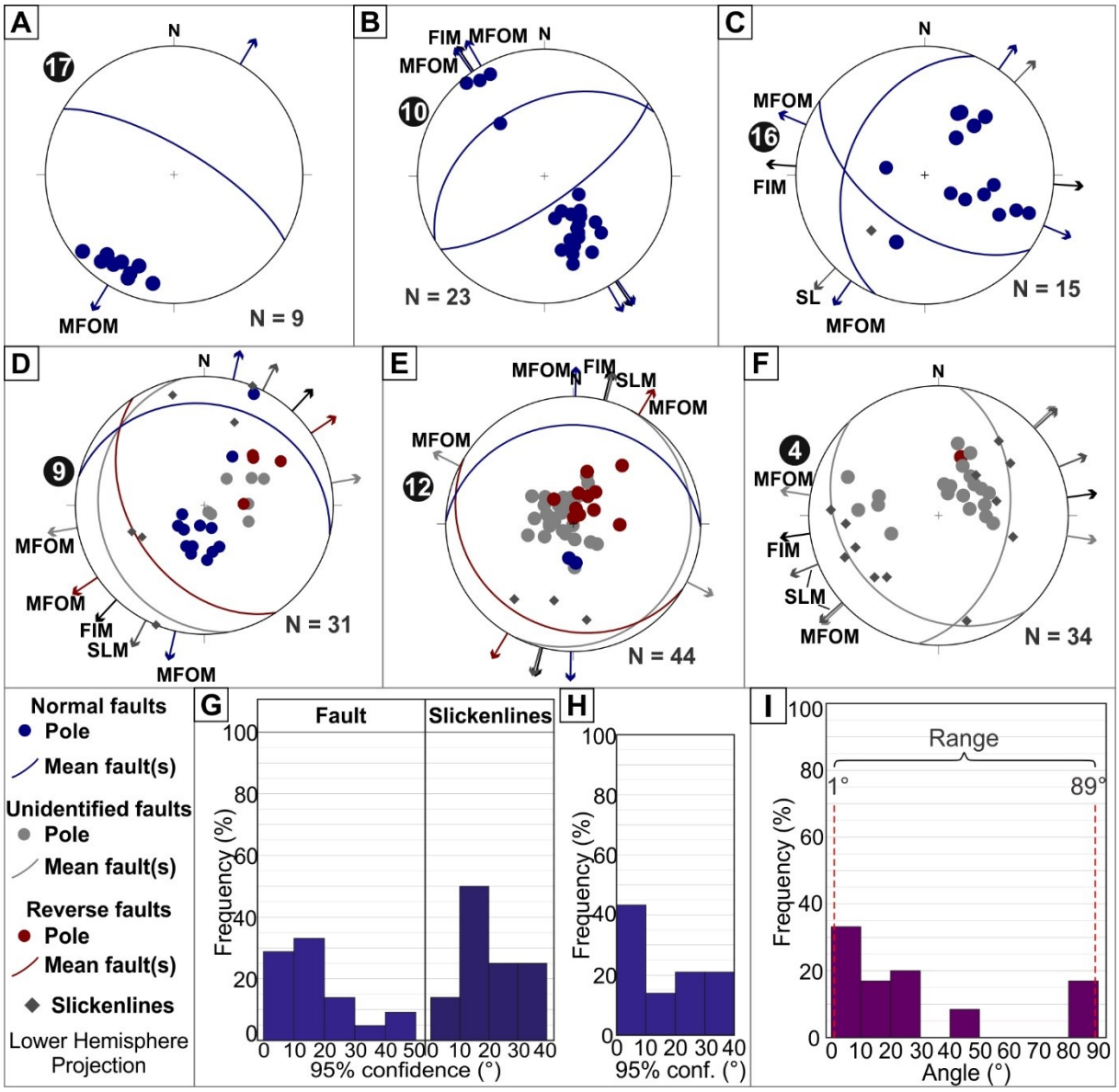
A
N
17
MFOM
N = 9
B
FIM MFOM N
MFOM
10
N = 23
C
N
MFOM
16
FIM
SL
MFOM
N = 15
D
N
9
MFOM
MFOM
FIM
SLM
MFOM
N = 31
E
MFOM FIM N SLM
MFOM
MFOM
12
N = 44
F
N
4
MFOM
FIM
SLM
MFOM
N = 34
Normal faults
Pole
Mean fault(s)
Unidentified faults
Pole
Mean fault(s)
Reverse faults
Pole
Mean fault(s)
Slickenlines
Lower Hemisphere Projection
G
Fault
Slickenlines
Frequency (%)
95% confidence (°)
H
Frequency (%)
95% conf. (°)
I
Range
1°
89°
Frequency (%)
Angle (°)

1496

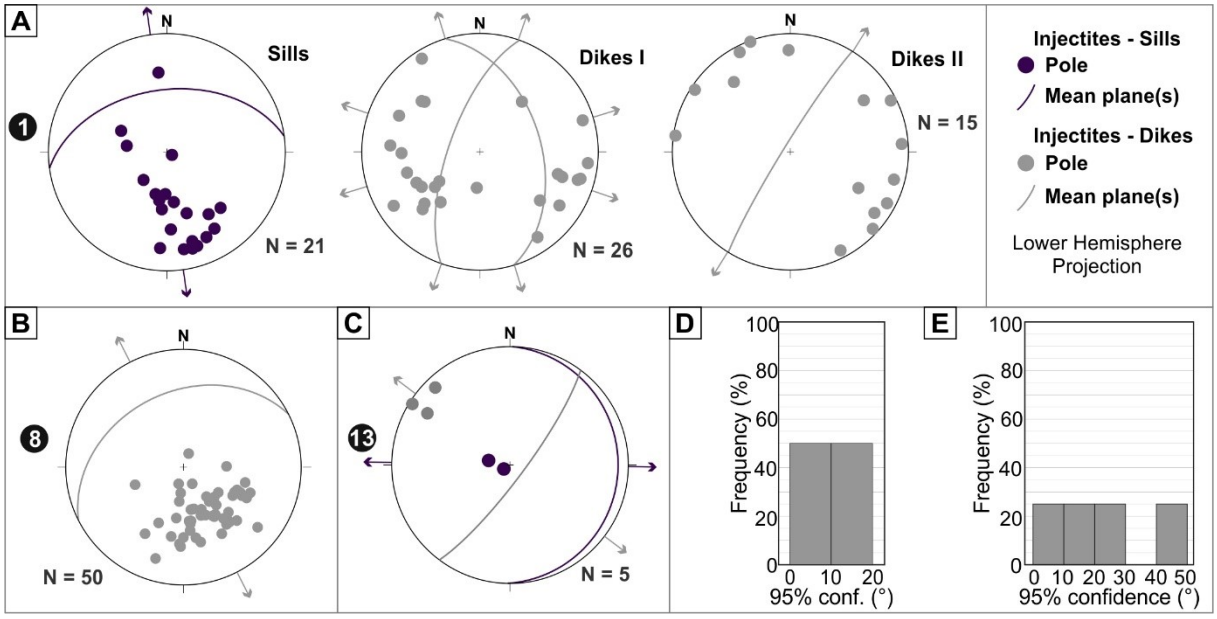
A
N
Sills
1
N = 21
N
Dikes I
N = 26
N
Dikes II
N = 15
Injectites - Sills
Pole
Mean plane(s)
Injectites - Dikes
Pole
Mean plane(s)
Lower Hemisphere Projection
B
N
8
N = 50
C
N
13
N = 5
D
Frequency (%)
95% conf. (°)
E
Frequency (%)
95% confidence (°)

1497

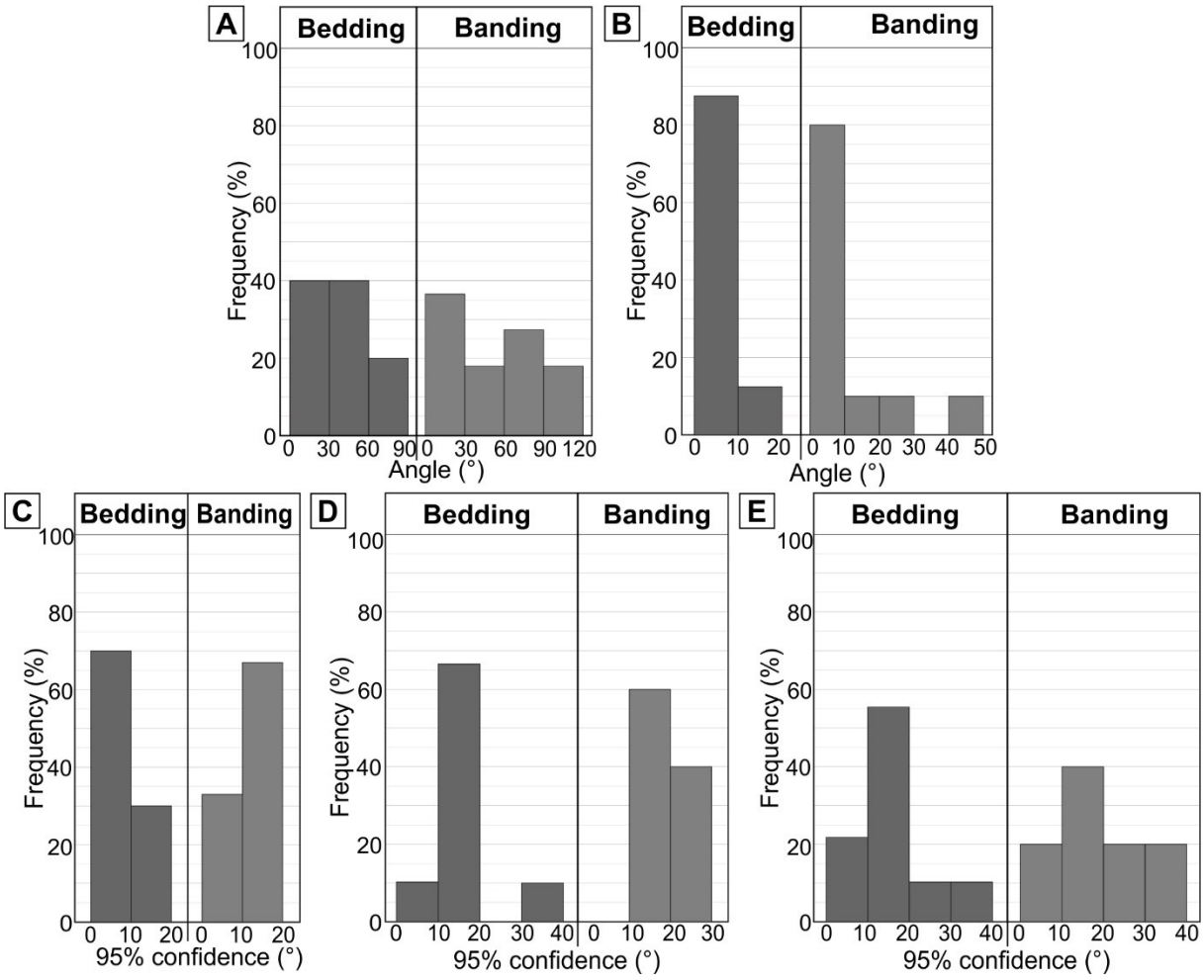
A
Bedding
Banding
Frequency (%)
Angle (°)
B
C
D
E
95% confidence (°)

1498

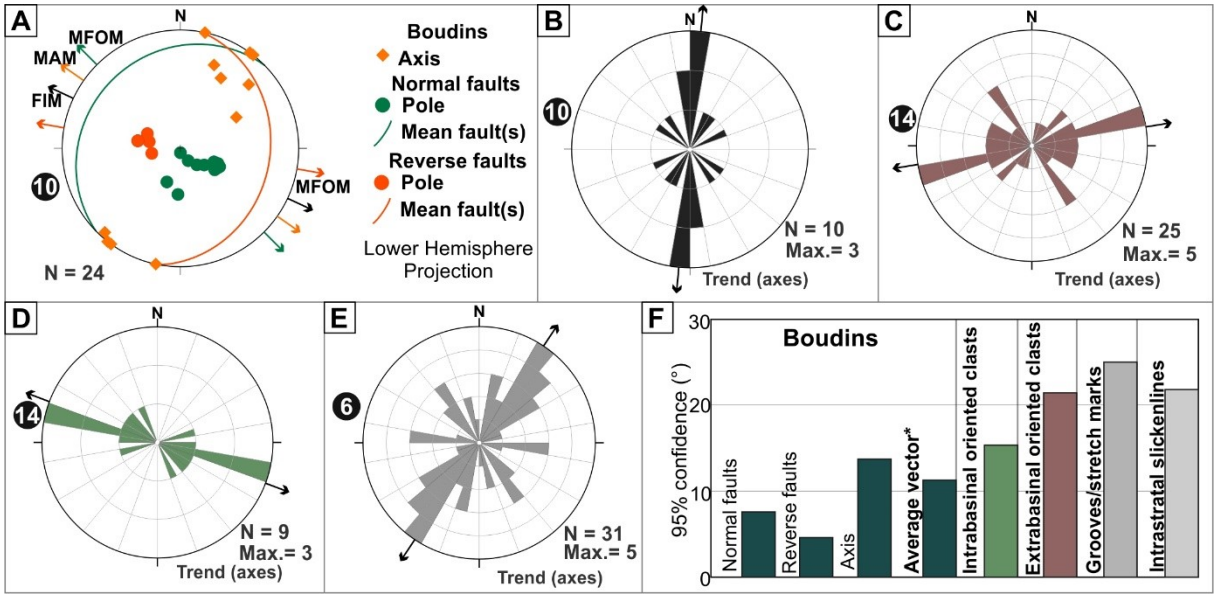
A
MFOM
MAM
FIM
N = 24
Boudins
Axis
Normal faults
Pole
Mean fault(s)
Reverse faults
Pole
Mean fault(s)
Lower Hemisphere Projection
B
N = 10
Max.= 3
Trend (axes)
C
N = 25
Max.= 5
Trend (axes)
D
N = 9
Max.= 3
Trend (axes)
E
N = 31
Max.= 5
Trend (axes)
F
Boudins
95% confidence (°)
Normal faults
Reverse faults
Axis
Average vector*
Intrabasinal oriented clasts
Extrabasinal oriented clasts
Grooves/stretch marks
Intrastratal slickenlines

1499

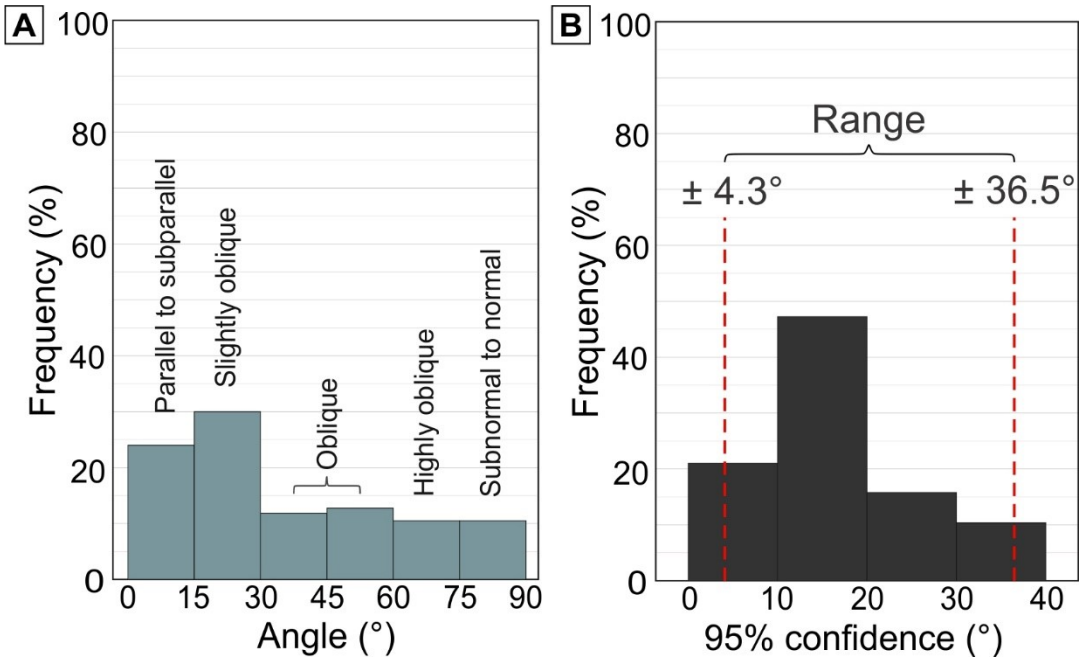
A
100
80
60
40
20
0
Frequency (%)
Parallel to subparallel
Slightly oblique
Oblique
Highly oblique
Subnormal to normal
0
15
30
45
60
75
90
Angle (°)
B
100
80
60
40
20
0
Frequency (%)
Range
± 4.3°
± 36.5°
0
10
20
30
40
95% confidence (°)

1500

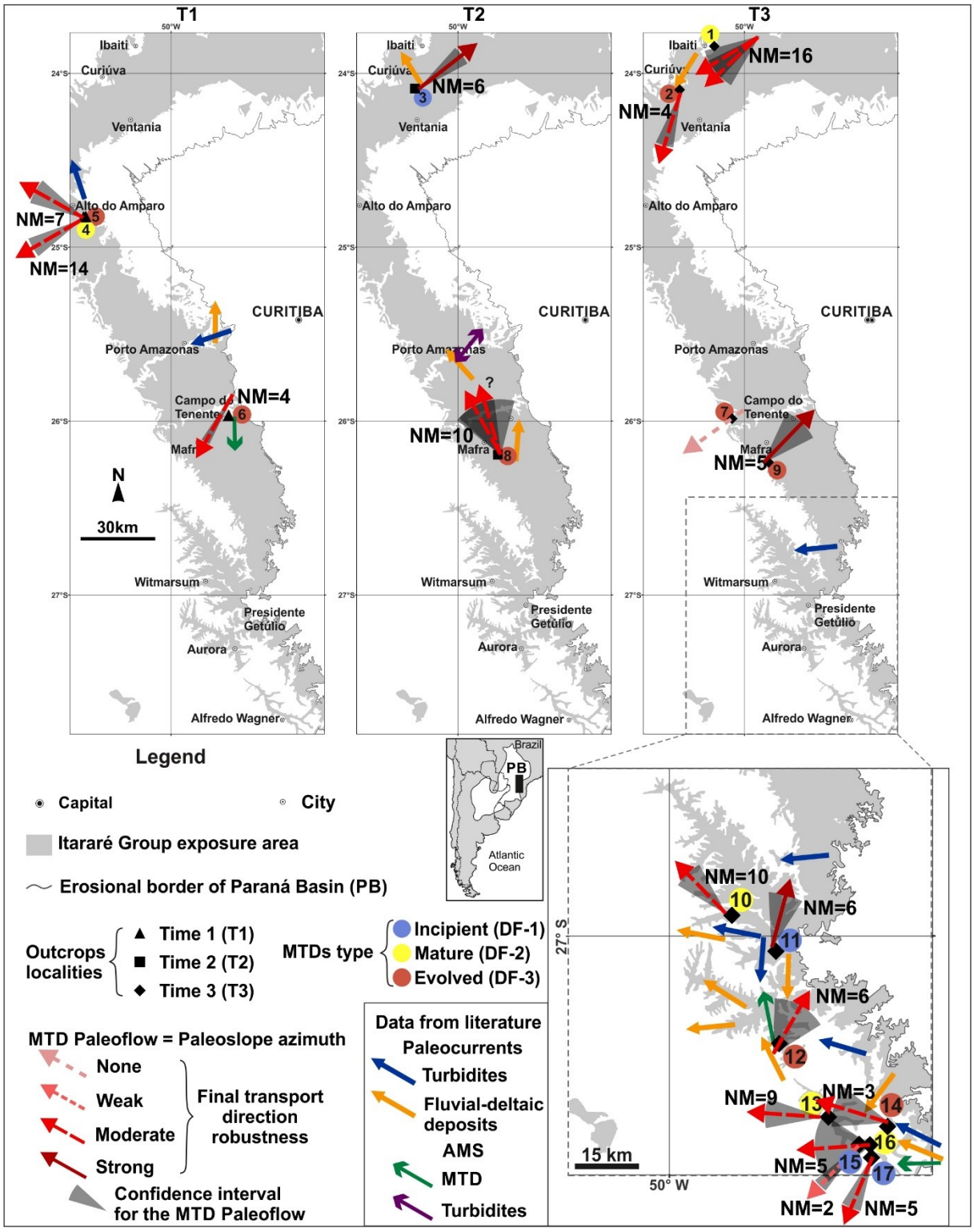
T1
T2
T3
Ibaiti
Curiúva
Ventania
Alto do Amparo
CURITIBA
Porto Amazonas
Campo do Tenente
Mafra
Witmarsum
Presidente Getúlio
Aurora
Alfredo Wagner
NM=7
NM=14
NM=4
NM=6
NM=10
NM=16
NM=5
N
30km
Legend
Capital
City
Itararé Group exposure area
Erosional border of Paraná Basin (PB)
Brazil
PB
Atlantic Ocean
Outcrops localities
Time 1 (T1)
Time 2 (T2)
Time 3 (T3)
MTDs type
Incipient (DF-1)
Mature (DF-2)
Evolved (DF-3)
MTD Paleoflow = Paleoslope azimuth
None
Weak
Moderate
Strong
Final transport direction robustness
Confidence interval for the MTD Paleoflow
Data from literature
Paleocurrents
Turbidites
Fluvial-deltaic deposits
AMS
MTD
Turbidites
27° S
50° W
15 km
NM=10
NM=6
NM=6
NM=9
NM=3
NM=5
NM=2
NM=5

1501

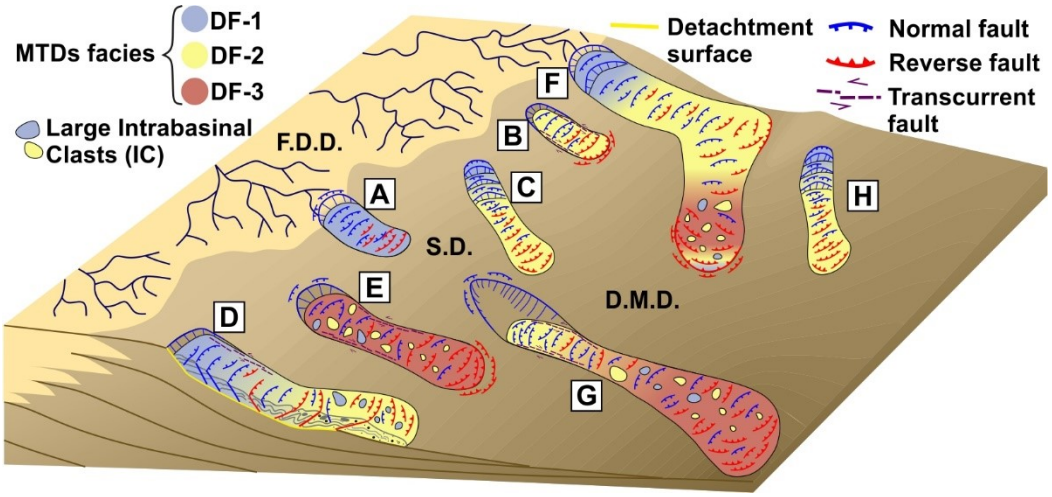
MTDs facies
DF-1
DF-2
DF-3
Large Intrabasinal Clasts (IC)
F.D.D.
S.D.
D.M.D.
Detachtment surface
Normal fault
Reverse fault
Transcurrent fault
A
B
C
D
E
F
G
H

1502